Astron. Astrophys. 270, 223–248 (1993)

ASTRONOMY AND ASTROPHYSICS

Light curves of Type Ia supernova models with different explosion mechanisms

A. Khokhlov[1 2], **E. Müller**[1], **and P. Höflich**[1]

[1] Max-Planck-Institut für Astrophysik, Karl-Schwarzschild-Str. 1, W-8046 Garching b. München, Germany
[2] Astronomical Institute, Moscow, Russia

Received August 28, accepted October 18, 1992

Abstract. Bolometric, blue and visual light curves are presented for a set of theoretical models for Type Ia supernovae including deflagration, detonation, delayed detonation, pulsating delayed detonation and tamped detonation scenarios.

The explosions are calculated using a one-dimensional Lagrangian code consistently with a nuclear reaction network (Khokhlov 1991b,c). For the calculations of the light curves a code is used (Höflich et al. 1992a,b) which is based on a LTE radiation transfer scheme (including both an energy equation for matter and radiation, and effects due to electron and line scattering). The transfer scheme implicitly solves the time-dependent, frequency averaged moment equations. The light curve code further contains a detailed equation of state with an elaborate treatment of the ionization balance and the ionization energies. Time-dependent expansion opacities (both Rosseland and Planck means) are used in a local approximation, which takes into account the composition structure of the explosion model. The code finally contains a Monte Carlo gamma-ray deposition scheme, which handles all relevant gamma-ray transitions and interaction processes.

We find that below a temperature of about 2 10^4 K the opacity rapidly drops from a value of $\gtrsim 0.1$ cm^2/g by more than an order of magnitude. This drop in opacity leads to a transition from the optically thick to the optically thin regime, which in turn determines to first order the time of maximum light. The transition occurs at different times in models with different expansion rates and structures. Consequently, the absolute value of the opacity does only weakly influence the time of maximum light as long as the opacity above the transition temperature is larger than ≈ 0.1 cm^2/g. This is in strict contrast to light curve models using a constant opacity. The light curves of the investigated models further strongly differ in their brightness at maximum light, the width of the maximum, and their post-maximum decline rate. These differences can be understood in terms of the expansion rate of the ejecta, the total energy release, the distribution of the radioactive matter, and the total mass and density structure of the envelope.

Several correlations between observable quantities and model parameters are found, which allow for a discrimination between models. For example, the maximum bolometric brightness decreases with the rise time t_{bol} and increases with the total mass of radioactive ^{56}Ni . The photospheric velocity at t_{bol} increases with L_{bol}.

Rise times to maximum bolometric luminosity longer than $\approx$ 15 days can hardly be provided by "standard" models (i.e., deflagrations, detonations or delayed detonations), but require "non-standard" models (i.e., pulsating delayed detonations or tamped detonations). These two classes of models can be distinguished by the time dependence of the expansion velocity at the photosphere v_{ph}, which is directly measurable by the Doppler shift of spectral lines. Contrary to the "standard" models, the "non-standard" models show a distinct plateau in v_{ph} after maximum whose width is determined by the envelope mass. The investigated "standard" models all have an absolute visual magnitude of $M_V = -19.68^m \pm 0.12^m$, while "non-standard" models have a systematically lower maximum brightness being as low as $M_V = -19.2^m$ and decreasing with increasing envelope mass. Thus, if the photospheric velocity shows a plateau, the supernova should be used with care when determining the Hubble constant.

Key words: supernovae and supernovae remnants: general – hydrodynamics – radiation transfer

1. Introduction

Nowadays it is widely accepted that Type Ia supernovae (SNe Ia) are thermonuclear explosions of degenerate stellar configurations (for recent reviews see Wheeler & Harkeness 1990; Woosley & Weaver 1992). Two major groups of theoretical models are discussed in the literature. The first group consists of massive carbon-oxygen white dwarfs with a mass close to the Chandrasekhar mass which accrete mass through Roche-lobe overflow from a companion star (Nomoto & Sugimoto 1977; Nomoto 1982). In these accretion models the explosion is trig-

Send offprint requests to: P. Höflich

gered by compressional heat released when the star adjusts to the accreted mass. The second group of models is the outcome of the merger scenario (Webbink 1984; Iben & Tutukov 1984; Paczyński 1985). In this scenario the orbit of a close binary system consisting of two intermediate-mass carbon-oxygen white dwarfs with a total mass above the Chandrasekhar mass decays due to the emission of gravitational waves, thus leading to a merging of the white dwarfs. During the merging process the less massive of the two dwarfs is destroyed forming an accretion disk around the more massive companion (Hachisu et al. 1986; Benz et al. 1989; Mochkovitch & Livio 1989, 1990).

Once ignited burning will propagate either in form of a detonation or a deflagration. In the detonation models (Arnett 1969; Hansen & Wheeler 1969) the thermonuclear burning front moves supersonically relative to the unburnt matter ahead of the front. This model only produces ^{56}Ni . In the deflagration models (Ivanova et al. 1974; Nomoto et al. 1976) the burning front propagates subsonically, i.e., matter ahead of the front can expand before it is consumed. Deflagration models produce both ^{56}Ni and intermediate mass elements (IME), a fact which has favoured these models in the past, because observations of SNe Ia require the production of some amount of IME to explain the spectra (see e.g., Wheeler & Harkness 1991).

In contrast to both of these single burning mode models the delayed detonation model recently proposed by Khokhlov (1991a) (see also Woosley & Weaver 1992; Shigeyama et al. 1992) assumes that an abrupt transformation from a deflagration to a detonation occurs during the explosion. The transition is either mediated by turbulent motion in the vicinity of the deflagration wave or by a strong pulsation of the white dwarf. The delayed detonation models do produce, contrary to the detonation and deflagration models, a substantial amount of both IME and Fe-group elements and they give an isotopic composition of Fe-peak elements which is compatible with that of the solar neighbourhood.

The different scenarios can be tested by comparison with observations. In particular, according to the idea of Colgate & McKee (1969) and Arnett (1979) that radioactive ^{56}Ni powers the light curve of SNe Ia, the measured absolute blue magnitude of SNe Ia in the Virgo cluster of $M_B = -19.79 \pm 0.12$ (Leibundgut & Tammann 1991) and, more recently, of $M_B = -19.6 \pm 0.4\ mag$ (Branch & Tammann 1992) implies a nickel mass of $M_{Ni}/M_\odot = 0.79 \pm 0.08$ and 0.63 ± 0.4, respectively.

Both analytical and numerical light curve models for SNe Ia have been studied during the last decade (for a review see e.g., Woosley & Weaver 1986, 1992; Wheeler & Harkness 1990). The physics incorporated into these models has increased in complexity, but the models still suffer from some more or less justified assumptions (e.g., diffusion approximation, constant opacity). Thus, we have decided to start a project to improve existing theoretical LC models (Höflich et al. 1991; Müller et al. 1991a; Khokhlov et al. 1991; Höflich et al. 1992a,b (henceforth H1 and H2)).

In the following we present an investigation of the light curves (LC) and photospheric velocities for a broad variety of models including "standard" ones (deflagration, detonation and delayed detonation models) and "non-standard" ones (pulsating delayed detonation and tamped, low density detonation models). The latter may be regarded as scenarios for merging WD or objects with a common envelope. The main question we address in this paper is whether different explosion models can be observationally discriminated on the basis of their light curves. In this context correlations between observable quantities and model dependent parameters are discussed in detail. In the next section we present the SN Ia models used in our analysis. In Sect. 3 we briefly describe our LC model and then discuss in detail the results of our bolometric and monochromatic LC calculations. Finally, in Sect. 4 the results are summarized and several conclusions are given.

2. Hydrodynamical models

As an input for our LC computations we use a set of SN Ia models which differ both in the explosion mechanism and the structure of the progenitor. All models have been computed using the technique described in Khokhlov (1991b,c).

2.1. Model construction

In a first step the hydrodynamics of the explosion is calculated for each model using a one-dimensional Lagrangian code, which is coupled with a simplified reaction network. Variations of the net electron mole fraction Y_e due to electron captures on free protons and NSE (nuclear statistical equilibrium) nuclei are calculated during the hydrodynamical evolution by means of a large NSE network using the capture rates of Fuller et al. (1982) and Takahashi et al. (1978). Thus, we take into account the change of the NSE binding energy with Y_e, which in turn influences the temperature and (consequently) the capture rates. In a second computational step the evolution of the chemical composition is post-processed with a large reaction network. The density, velocity and (final) chemical composition profiles are the input for the light curve computations.

In SNe Ia basically two modes of flame propagation are possible: detonations (supersonic mode in which matter is ignited by a strong shock) and deflagrations (subsonic mode in which the flame propagates due to heat transport). The velocity of a detonation (Chapman-Jouguet velocity) is well defined and for a degenerate mixture of C/O is in the range of $1.1 - 1.4\ 10^9$cm sec^{-1} depending on density. Therefore, the outcome of a detonation is fixed by the assumed initial conditions. Given the mass and the chemical composition of a WD the result of a detonation can be predicted fairly well.

For deflagrations the velocity of flame propagation is not well known. It must be larger than a lower limt given by the velocity of a laminar deflagration D_l (heat transport by thermal conductivity only), which in degenerate matter is about $\simeq 10^{-2}$ of the sound velocity a_s (Woosley & Timmes 1992). The velocity of a steady deflagration must also be smaller than the Chapman-Jouguet deflagration velocity $D'_{\rm CJ} \simeq (0.3 - 0.6)a_s$ depending on density (Khokhlov 1988). Since deflagrations in

Table 1. Overview of investigated SN Ia models. The quantities given in columns 3 to 11 are the white dwarf mass M_*, the central density ρ_c, the ratio of deflagration velocity and local sound speed α, the transition density at which the deflagration is assumed to turn into a detonation ρ_{tr}, the final kinetic energy E_{kin}, the mass of synthesized ^{56}Ni M_{Ni}, the average expansion velocity $< v >$, and the number of radial zones N_r. In model DF1MIX the composition was completely homogenized after burning had stopped.

Model	Mode of explosion	M_* [$M_\odot$]	ρ_c [10^9 gcm^{-3}]	α	ρ_{tr} [10^7 gcm^{-3}]	E_{kin} [10^{51} erg]	M_{Ni} [$M_\odot$]	$< v >$ [10^8 cm/s]	N_r
DET1	detonation	1.4	3.5	—	—	1.75	0.92	10.1	100
DF1	deflagration	1.4	3.5	0.30	—	1.10	0.50	8.3	100
DF1MIX	deflagration	1.4	3.5	0.30	—	1.10	0.50	8.3	100
W7	deflagration	1.2	2.0	n.a.	—	1.30	0.53	8.9	170
N21	delayed det.	1.4	3.5	0.03	5.0	1.63	0.83	9.3	500
N32	delayed det.	1.4	3.5	0.03	2.6	1.52	0.56	8.9	100
PDD3	pulsating delayed det.	1.4	2.1	0.04	2.0	1.37	0.49	9.1	500
DET2	detonation	1.2	0.04	—	—	1.52	0.63	10.3	500
DET2ENV2	det. + envelope	1.2 + 0.2	0.04	—	—	1.52	0.63	9.4	472
DET2ENV4	det. + envelope	1.2 + 0.4	0.04	—	—	1.52	0.63	8.7	508
DET2ENV6	det. + envelope	1.2 + 0.6	0.04	—	—	1.52	0.63	8.2	600

SNe Ia are subject to Rayleigh-Taylor instabilities (see, e.g., Müller & Arnett 1982, 1986) and might become turbulent, the effective flame velocity can be larger than the corresponding laminar velocity due to an increase of the effective surface of the flame. Without a quantitative theory of turbulent deflagrations any value from D_l to $D'_{\rm CJ}$ is admissible. In our study we assume that the deflagration velocity is equal to a fraction α of the local sound speed in front of the flame front, i.e.,

$$D_{def} = \alpha \cdot a_s \ . \qquad (1)$$

Some care is required when incorporating Eq. (1) into a hydrodynamical code. The details of our implementation which is based on an artificial limiting of the burning rate and which allows us to avoid small scale temperature fluctuations is given in Appendix A.

The complete list of our models is given in Table 1. The density, velocity and chemical profiles of the ejecta after burning becomes quenched and free expansion is established are shown in Figs. 1 to 7. The yields of the models are listed in Table 2.

Table 2. Yields (in $M_\odot$) for various SN Ia models.

Element	DET1	DF1	N32	N21	PDD3	DET2
He	$3.9\ 10^{-3}$	$2.6\ 10^{-5}$	-	$6.4\ 10^{-3}$	-	$1.8\ 10^{-3}$
C	-	0.130	$7.2\ 10^{-3}$	$7.0\ 10^{-3}$	0.100	$6.0\ 10^{-3}$
O	$9.5\ 10^{-3}$	0.199	$9.8\ 10^{-2}$	$4.2\ 10^{-2}$	0.143	$6.6\ 10^{-2}$
Ne	-	$8.8\ 10^{-3}$	$1.4\ 10^{-3}$	$3.1\ 10^{-4}$	$5.9\ 10^{-3}$	$3.6\ 10^{-4}$
Na	-	$2.4\ 10^{-4}$	-	-	$1.2\ 10^{-4}$	-
Mg	$5.1\ 10^{-4}$	$8.3\ 10^{-3}$	$5.1\ 10^{-3}$	$1.7\ 10^{-3}$	$1.0\ 10^{-3}$	$2.9\ 10^{-3}$
Si	$3.6\ 10^{-3}$	$3.3\ 10^{-2}$	0.227	0.122	0.174	0.184
P	$2.7\ 10^{-5}$	$3.9\ 10^{-4}$	$3.3\ 10^{-4}$	$1.0\ 10^{-4}$	$2.7\ 10^{-4}$	$2.0\ 10^{-4}$
S	$1.1\ 10^{-3}$	$1.6\ 10^{-2}$	0.155	$8.2\ 10^{-2}$	0.131	0.121
Cl	-	$9.8\ 10^{-5}$	$9.5\ 10^{-5}$	$2.3\ 10^{-5}$	$8.6\ 10^{-5}$	$5.4\ 10^{-5}$
Ar	$2.2\ 10^{-4}$	$3.0\ 10^{-3}$	$3.5\ 10^{-2}$	$1.9\ 10^{-2}$	$3.2\ 10^{-2}$	$2.6\ 10^{-2}$
K	-	$5.3\ 10^{-5}$	$4.0\ 10^{-5}$	$1.1\ 10^{-5}$	$5.1\ 10^{-5}$	$2.1\ 10^{-5}$
Ca	$4.7\ 10^{-4}$	$1.7\ 10^{-3}$	$3.9\ 10^{-2}$	$2.1\ 10^{-2}$	$3.7\ 10^{-2}$	$2.8\ 10^{-2}$
Sc	-	-	-	-	-	-
Ti	$7.6\ 10^{-5}$	$1.2\ 10^{-4}$	$3.0\ 10^{-3}$	$2.6\ 10^{-3}$	$9.8\ 10^{-4}$	$7.2\ 10^{-4}$
V	$5.1\ 10^{-5}$	$7.5\ 10^{-5}$	$3.0\ 10^{-4}$	$2.3\ 10^{-4}$	$1.8\ 10^{-4}$	$1.0\ 10^{-4}$
Cr	$6.4\ 10^{-3}$	$2.1\ 10^{-2}$	$4.8\ 10^{-2}$	$3.7\ 10^{-2}$	$2.7\ 10^{-2}$	$1.7\ 10^{-2}$
Mn	$1.7\ 10^{-2}$	$1.9\ 10^{-2}$	$1.3\ 10^{-2}$	$9.3\ 10^{-3}$	$1.4\ 10^{-2}$	$6.0\ 10^{-3}$
Fe	1.193	0.828	0.740	0.985	0.681	0.702
Co	$4.4\ 10^{-4}$	$1.2\ 10^{-3}$	$6.1\ 10^{-4}$	$1.0\ 10^{-4}$	$3.7\ 10^{-4}$	$1.9\ 10^{-4}$
Ni	0.176	0.139	$3.7\ 10^{-2}$	$7.4\ 10^{-2}$	$5.0\ 10^{-2}$	$3.1\ 10^{-2}$

Models DET1, DF1, DF1MIX, N21, N32 and PDD3 are thermonuclear explosions of a massive degenerate C/O dwarf of $1.4M_{\odot}$. All explosions are assumed to start near the center. We have also investigated thermonuclear explosions of C/O configurations of different mass. This latter set of models consists of an explosion model of a bare C/O dwarf with a mass of $1.2M_{\odot}$ (DET2) and of three models (DET2ENV2, DET2ENV4, an extended low density C/O envelope. These models crudely mimic configurations which might occur after merging of two C/O white dwarfs. Note that the value of $1.2M_{\odot}$ can be varied inside a certain range (see below) but it is chosen to allow for a comparison with the delayed detonation model PDD3 .

2.2. Detonation model DET1

In model DET1 the detonation wave converts almost all material into NSE iron group elements and produces virtually no IME. The star only begins to expand after the detonation reaches its surface $\simeq$ 0.3 s after ignition. During the next $\simeq$ 10 s almost all thermal energy released during burning is converted into kinetical energy of the ejecta, which then expand freely. The final density and velocity profiles are shown in Fig. 1. A typical feature of the profiles is a gradual increase of the velocity and a gradual decrease of the density with mass. This is mainly due to the uniform deposition of released nuclear energy inside the star. After the detonation wave has reached the surface the specific thermal energy is almost constant (including the energy which is released during the first few tenths of a second of the expansion due to NSE rearrangement of nuclei).

2.3. Deflagration model DF1

In the deflagration model DF1 burning propagates outwards as a subsonic flame (deflagration) with a velocity of $0.3a_s$ (see Table 1). Thus, the star already expands during flame propagation and burning ceases before all C/O is converted into Fe-peak elements, i.e., the outer layers of the WD remain unburnt. IME are synthesized in the region where the deflagration wave becomes quenched. This layer of IME separates the NSE core from the outer unburnt envelope (Fig. 2).

The final velocity and density profiles of model DF1 differ substantially from those of the detonation model DET1. In

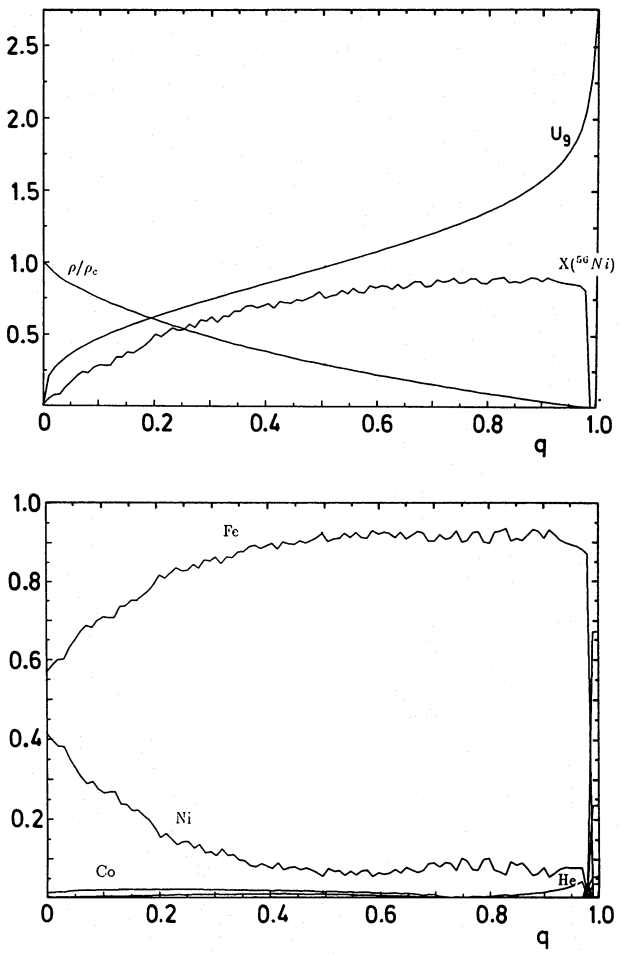

Fig. 1. Density (in units of the central density), velocity (in units of 10^9 cm/s), initial ^{56}Ni mass fraction (top) and final composition (bottom) of model DET1 as a function of mass coordinate $q = M(r)/M_*$

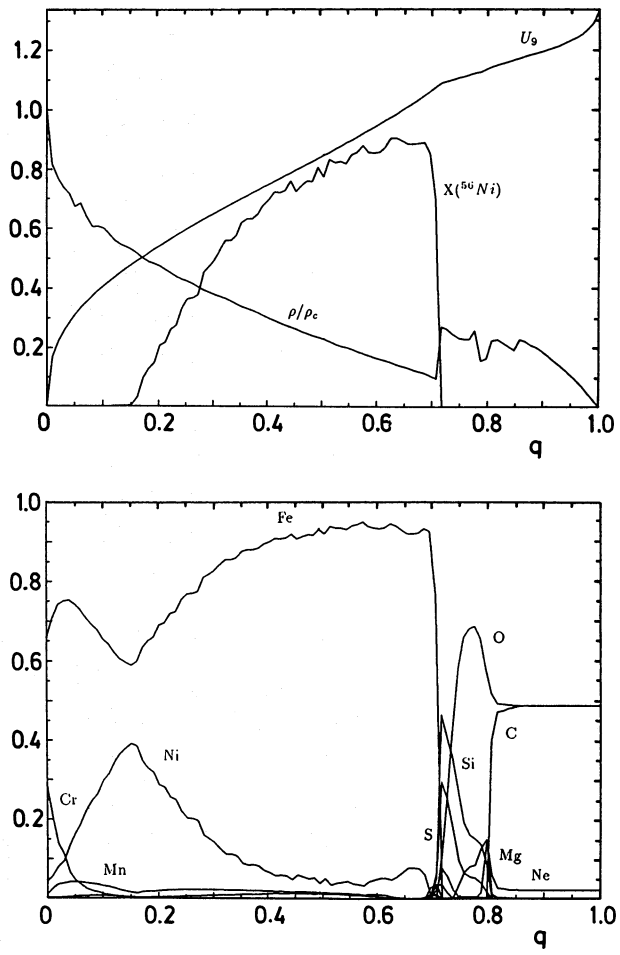

Fig. 2. Same as Fig. 1 but for model DF1

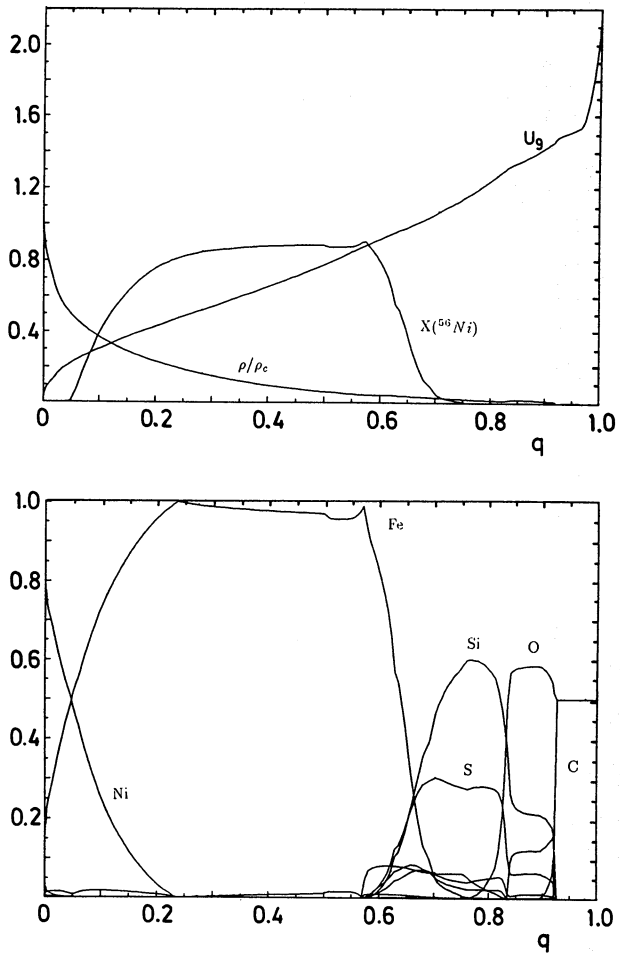

Fig. 3. Same as Fig. 1 but for model W7

model DF1 there is no nuclear energy input into the unburnt outer layers and, thus, they are accelerated due to the interaction with the rapidly expanding, underlying core of Fe-peak elements. This interaction leads to the formation of a density bump at $q \simeq 0.7$ and flattens the velocity profile in the outer layers ($q \gtrsim 0.7$, Fig. 2).

The formation of IME is in general agreement with observations. However, in model DF1 these elements are confined to a thin mass layer, i.e., they are spread only over a narrow velocity range of $\simeq$ 1000 km/s. Spectral observations indicate on the other hand that in SNe Ia IME are moving with velocities ranging from $\simeq$ 10000 to $\simeq$ 20000 km/s and even more (e.g., Branch 1982, Leibundgut et al. 1991b).

The formation of IME in a thin layer can be explained as follows. Burning starts near the center, but due to the subsonic nature of a deflagration wave the released energy is transported to the outer layers by pressure waves. Very soon after ignition the star expands with a velocity increasing with radius. The expansion velocity gradually increases with time. When the flame reaches the layers where IME begin to form, the expansion velocity becomes comparable with or even exceeds the flame velocity. As a result the density ahead of the moving flame rapidly decreases and the flame becomes quenched before much IME are produced. Models with different parameter $\alpha = D_{def}/a_s \lesssim 0.4 - 0.5$ show a similar behaviour. They only differ by the position where the layer of IME is located. Models with larger α give rise to a detonation in the steep density gradient near the surface due to the steepening of pressure waves into a shock (Woosley & Weaver 1992, Khokhlov 1991b).

The border between burnt and unburnt matter in model DF1 is Rayleigh-Taylor unstable. Thus, some mixing of Fe-peak and IME with unburnt C/O matter should be expected. However, the R-T mixing is not effective enough to accelerate IME up to velocities of $\simeq$ 20000 km/s (Sutherland & Wheeler 1984). Assuming that the observed velocity spread of IME is due to some other yet unknown mixing process, does only shift the problem, because one then must also explain, why this mixing process was less effective during flame propagation and allowed the flame to become quenched. Considering models with an initially very small α which increases with radius also does not solve the problem. The smaller α the more effectively burning causes a global expansion of the star. Moreover, starting with an initially small α requires a much larger (then for the case of a constant α) deflagration velocity to incinerate any reasonably large fraction of the star (Woosley et al. 1986, see also discussion in Khokhlov 1991b,c). Then one runs into the problem that $D_{def} \leq D'_{\rm CJ}$ (see Sect. 2.1) and that pushing D_{def} beyond this limit usually causes the formation of a detonation due to the steepening of outgoing shock/pressure waves.

To our knowledge model W7 of Nomoto et al. (1976, 1984) is the only deflagration model in the literature which is characterized by D_{def} varying from a very subsonic value ($\simeq 0.01 a_s$) to a value beyond the limiting CJ deflagration velocity and which, as the authors claim, does produce substantial amounts of both Fe-peak and IME for a wide velocity range (see Fig. 3). We were not able to reproduce this result with our hydrodynamical code. Using the prescription of the flame velocity of model W7 in our code leads to a much larger expansion rate and a much stronger density decrease than reported by Nomoto et al. (1984). Variations of the burning law did not help to obtain their result. The main reason for this discrepancy may be the use of an implicit hydrodynamical code by Nomoto et al. (1984) with a time step grossly exceeding the one required by the CFL condition (large time steps are necessary to ensure the numerical stability of their code, which becomes unstable with decreasing δt). Large time steps (in comparison with the sound crossing time) would effectively suppress an expansion of the outer layers occuring on a hydrodynamical time scale and, thus, would produce an incorrect hydrodynamical behaviour of the exploding star (see also Sect. 2.5). Recently, Yamaoka et al. (1992) have calculated a new delayed detonation model called 'late detonation' model W7 by the authors. The behaviour of the new model qualitatively resembles our delayed detonation model N32 including the composition inversion (see next section). The difference between model N32 and the 'late detonation' model W7 is the location of the composition inversion. and that model N32 expands with somewhat larger velocities, because of the non-constant α assumed by Yamaoka et al. (1992). In conclusion, the origi-

nal model W7 is not a hydrodynamically self-consistent SN Ia model and, due to this fact, the velocity and density structure of the model are not consistent with the composition structure.

2.4. *Delayed detonation models N21 and N32*

In contrast to the (single burning mode) detonation and deflagration models the delayed detonation model (Khokhlov 1991a,b) utilizes the idea that an abrupt transition from a deflagration to a detonation may occur during the explosion of a white dwarf. The transition can either occur due to turbulent motion in the vicinity of the deflagration wave or due to a strong pulsation of the WD during the explosion (see next section).

To allow for the formation of a detonation wave, a non-uniformly pre-heated region must be created with a size exceeding some critical value. The non-simultaneous explosion of this region and the resulting cumulative interaction of pressure waves and burning inside this region then give rise to a detonation. Although the growth of pressure waves into a detonation inside a given non-uniformly pre-heated region can be computed rather easily (Khokhlov 1991a), the formation of such a region is a very complicated process which involves turbulent mixing of fresh fuel and burning products in the vicinity of the propagating or quenched (in case of a pulsation; see next section) flame front. This process cannot be modeled with present-day computers. Thus, in our models the transition is imposed artificially when some critical density ρ_{tr} is reached.

Models N21 and N32 are examples for delayed detonation models, in which the transition between deflagration and detonation occurs in the vicinity of a slowly moving deflagration front. During the deflagration phase the WD expands and its density decreases. Then the deflagration turns into a detonation, which incinerates the outer layers of the WD. As the detonation propagates through pre-expanded layers of low density, it produces a significant amount of IME (Imshennik & Khokhlov 1984).

While the progenitor and the flame parameter $\alpha = 0.3$ are the same for models N21 and N32, they differ in the density ρ_{tr} at which the transition from a deflagration to a detonation is assumed. In model N21 $\rho_{tr} = 5\ 10^7$ gcm^{-3}, i.e., the detonation synthesizes a significant amount of ^{56}Ni in layers with $\rho \simeq 1 - 5\ 10^7$ gcm^{-3}. In layers with $\rho \lesssim 10^7$ gcm^{-3}the detonation produces mostly IME. In model N32 the transition density is lower ($\rho_{tr} = 2.6\ 10^7$ gcm^{-3}). As a result less ^{56}Ni is produced and the amount of synthesized IME is larger. In model N21 the IME are distributed in a velocity range $\sim$ 12000 – 30000 km/s (Fig. 4), whereas in model N32 the IME move with velocities $\lesssim$ 10000 km/s (Fig. 5). Note that in model N32 the transition occurs

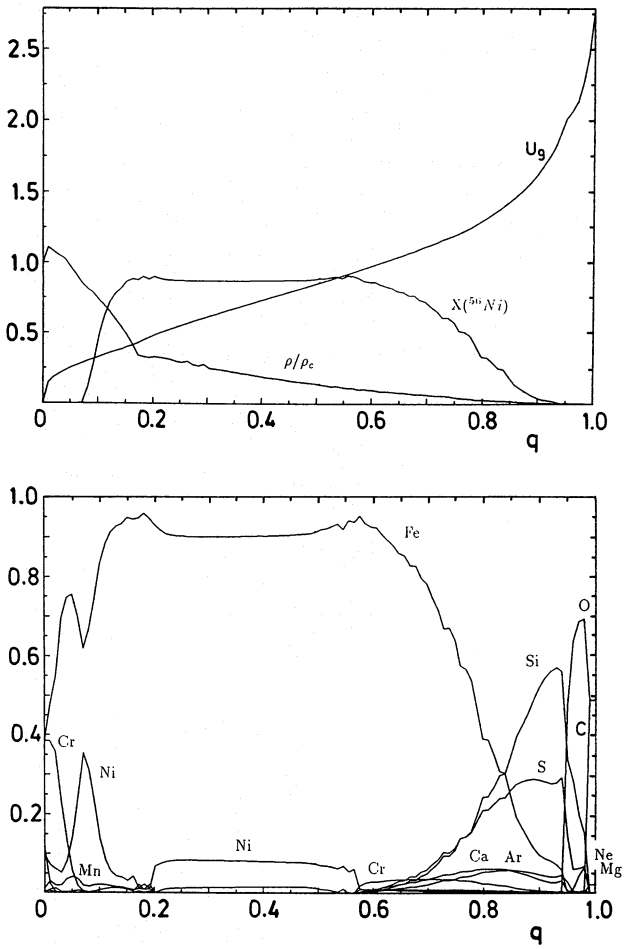

Fig. 4. Same as Fig. 1 but for model N21

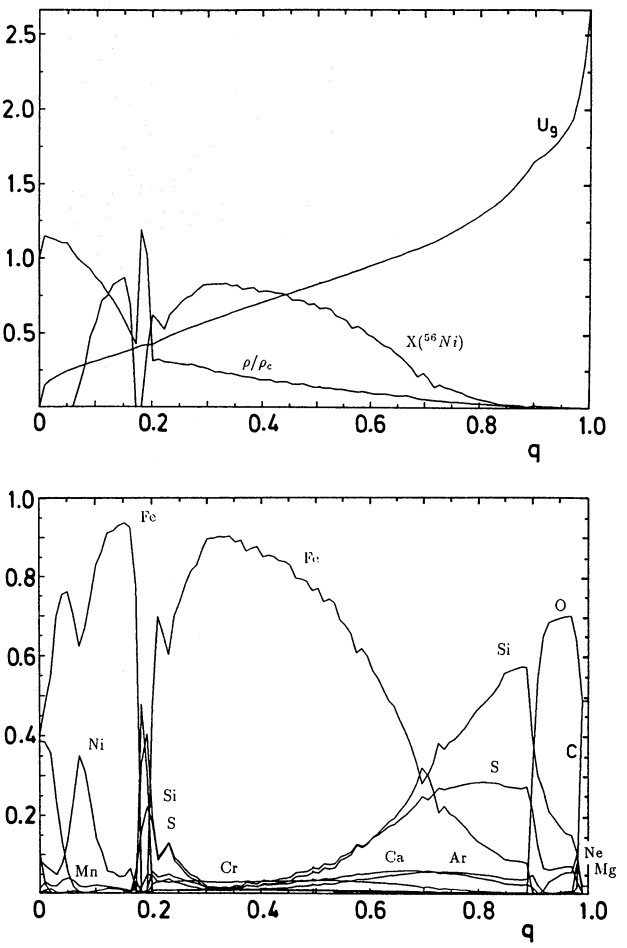

Fig. 5. Same as Fig. 1 but for model N32

when the deflagration is about to become quenched and and to produce IME. Switching to a detonation raises the temperature, i.e., ^{56}Ni is produced again. This explains the formation of a thin layer of IME at $q \simeq 0.2$ sandwiched between layers containing Fe-peak elements (Fig. 5). In both models Fe-peak elements and IME coexist in a rather wide range of expansion velocities. This is in contrast to model DF1 and is characteristic for the nucleosynthesis occuring in a detonation wave.

Although the ^{56}Ni -production in model N32 only reaches 67% of that in model N21 (see Table 1) the kinetic energies of the ejecta differ only marginally ($\simeq$ 10%). This illustrates the general fact that the ^{56}Ni -production during the explosion is not closely correlated with the kinetic energy of the ejecta. The central hole in the ^{56}Ni -distribution is caused by neutronization occuring more effectively at high densities and temperatures. The size of the hole depends on the regime of flame propagation and, thus, the amount of ^{56}Ni -underproduction near the center is model dependent (see discussion below).

The density and velocity profiles of models N21 and N32 are similar and resemble those of detonation model DET1 (Figs. 1, 4 and 5). Moreover, as in the former models the explosion completely incinerates the WD, no interaction of an expanding hot core with an unburnt envelope occurs. Thus, in contrast to model DF1 no velocity plateau is formed in models N21 and N32 (see Figs. 2, 4 and 5).

2.5. *Pulsating delayed detonation model PDD3*

Two arguments favor a low ($D_{def} \simeq 0.01 - 0.03\, a_s$) flame velocity near the WD center. First, such a low velocity helps to avoid overproduction of some neutron-rich Fe-isotopes, in particular ^{54}Fe (Woosley et al. 1986, Khokhlov 1991c). Second, a low velocity is expected near the WD center on theoretical grounds, because the R-T instability is ineffective near the center (Woosley 1990).

If a deflagration wave propagates with a velocity $D_{def} \lesssim 0.06 a_s$ and no transition to a detonation wave occurs the deflagration wave becomes quenched before the total binding energy of the star becomes positive. The WD remains bound and experiences a strong pulsation. During the contraction phase of the pulsation burning can set in again. If this happens in form of a deflagration the star becomes unbound after a few more percent of its mass is burnt. The ejecta move with low velocity ($\simeq$ 1000 km/s) and are mainly composed of C/O with a small amount of ^{56}Ni and IME in the inner parts. Thus, a subluminous and red SN Ia would be the outcome. However, a simple estimate shows that during the pulsation a mixed layer with a size of a few 10^8 cm should form at the border between the unprocessed and the processed material. Adiabatic compression of this high entropy layer will probably give rise to a detonation in pulsating delayed detonation models like PDD3 (Khokhlov 1991c; Höflich et al. 1992b).

The hydrodynamics of pulsating delayed detonations differs essentially from that of genuine delayed detonations. Computations show that the pulsation is highly non-homologous for a rather long time ($\approx$ 100 sec): The outermost layers continue to expand, while the infalling matter eventually forms an inward moving strong shock wave. The detonation wave which has been initiated in model PDD3 at $\rho_{tr} = 1.7\ 10^7\ gcm^{-3}$ propagates through matter falling towards the center with velocities $u \simeq -2\ 10^8$ cm/s. This is in contrast with simple delayed detonation models like N21 and N32 in which the detonation propagates through an already expanding envelope. Thus, the detonated matter appears somewhat decelerated in model PDD3 compared to a delayed detonation without a pulsation. The detonation transforms into a strong shock at densities below $\lesssim 10^5$ gcm^{-3} when the time scale of nuclear burning becomes large compared to the hydrodynamic time scale. This blast wave collides with an incoming shock formed due to the collapsing envelope the relative velocity being larger than 10^9 cm/s. The interaction lasts for $\sim$ 10 s, because of the large size of the envelope. Subsequently a reflected shock wave propagates deep into the WD. This results in a substantial deceleration of the bulk of the processed matter and in a flat velocity profile for $q \lesssim 0.85$ with a mean velocity $\lesssim$ 10000 km/s. The outer layers acquire high velocities of up to 20000 – 30000 km/s (Fig. 6).

The interaction between the expanding matter and the envelope in pulsating delayed detonation models has two more

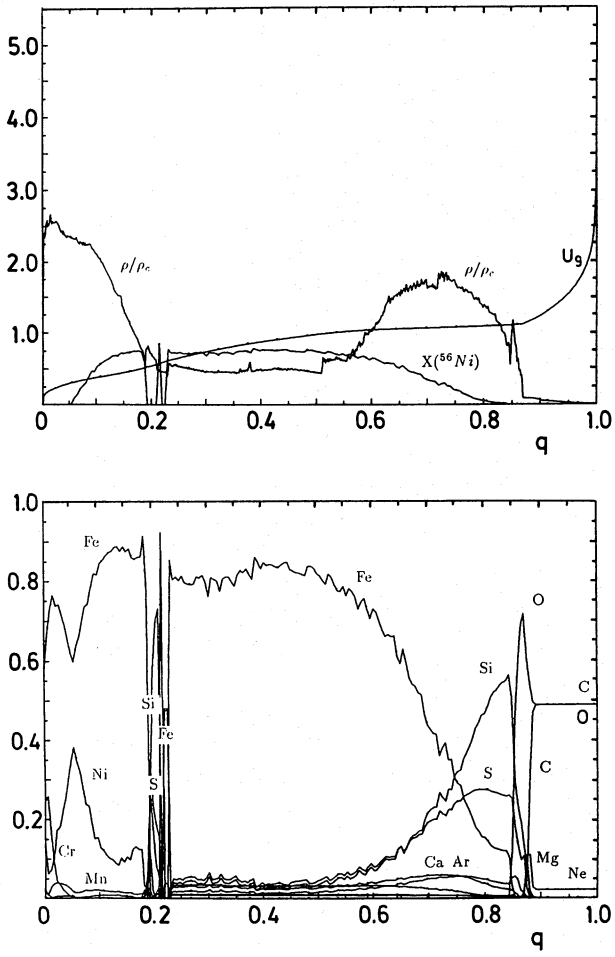

Fig. 6. Same as Fig. 1 but for model PDD3

important consequences. *Firstly*, the interaction region is characterized by a large density and pressure gradients of opposite sign, i.e., the region $q \gtrsim 0.7$ is Rayleigh-Taylor unstable. In contast to single mode deflagration models strong mixing of the outer $\simeq$ 30% of the envelope may be expected. *Secondly*, a reverse shock wave is formed by the interaction which creates a shell-like density distribution and a very fast expanding envelope around this shell.

The structure of the progenitor and the flame velocity during the deflagration stage are similar in model PDD3 to the low velocity deflagration model computed by Nomoto et al. (1976). The hydrodynamical response of the outer layers of model PDD3 on the energy release near the center differs, however, from that found by Nomoto et al. (1976). In their case the pulsation is homologous and no reverse shock is formed, This is probably caused by numerical damping of hydrodynamical motions, which is unavoidable when using an implicit hydro-code with time steps much larger than the corresponding CFL time step. The damping is probably also responsible for the discrepancies between our and Nomoto et al. 's (1984) calculations of model W7 (see Sect. 2.3). We further point out that a high resolution of the outer layers of model PDD3 is crucial even if an explicit hydro-code is used, because otherwise the reverse shock formation is described inadequately. Close to the center the early evolution of model PDD3 and that of the model of Nomoto et al. (1976) agree well.

Finally, we mention that pulsations of exploding white dwarfs have been obtained previously by Ivanova et al. (1974, 1977) and Chechetkin et al. (1980). In their models the flame front propagated due to compressional heating caused by pulsations leading in some cases to the formation of detonation waves. These results have been criticized by Nomoto & Sugimoto (1977) who pointed out that the computations were severely affected by a numerical generation of entropy. Ivanova et al. (1982) responded that this entropy generation was caused by weak shock waves formed during flame propagation, but later admitted that the entropy production was of numerical origin and finally came to the conclusion that 'the burning never proceeded through the detonation regime' (Ivanova et al. 1983). For a more detailed discussion of these points see Khokhlov (1991b).

2.6. Low density detonation model DET2 and tamped detonation models DET2ENV2, DET2ENV4, DET2ENV6

According to the merger scenario (Webbink 1984; Iben & Tutukov 1984; Paczyński 1985) a white dwarf surrounded by an extended envelope (which resembles the dynamically "accreted" binary companion) may be considered as a SN Ia progenitor (Hachisu et al. 1986; Benz et al. 1989; Mochkovitch & Livio 1989, 1990). As such models may be tested on the basis of their light curves (and spectra) we have calculated three models (DET2ENV2, DET2ENV4 and DET2ENV6) which consist of an intermediate mass C/O white dwarf ($M_* = 1.2\ M_\odot$; $\rho_c = 4\ 10^7$ gcm^{-3}) detonating inside a low-density C/O envelope ($\rho \propto r^{-2}$ and $R_{env} = 10^{10}$ cm) of 0.2 $M_\odot$, 0.4 $M_\odot$ and

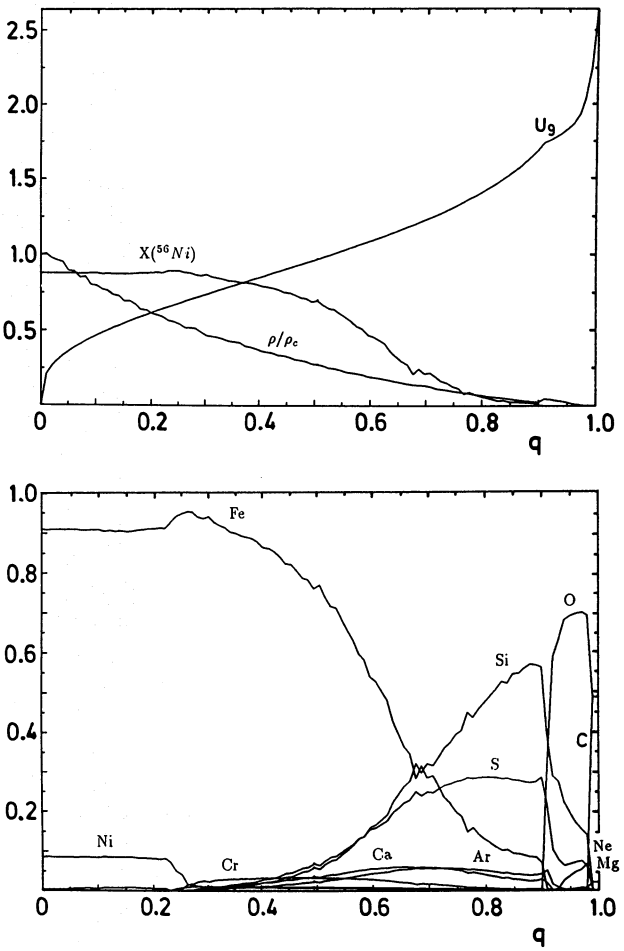

Fig. 7. Same as Fig. 1 but for model DET2

0.6 $M_\odot$, respectively. The density of the envelope is low, i.e., matter in the envelope does not burn. Model DET2 represents the explosion of the same dwarf in the absence of an envelope. Note that in a different context a similar type of 'tamped detonation' models (with helium envelopes) have been investigated by Woosley et al. (1986).

The hydrodynamical behaviour, the density and velocity profiles of model DET2 are similar to those of model DET1 (Figs. 1 and 7). However, the resulting chemical composition is quite different. Due to the low central density of the white dwarf, the detonation in model DET2 produces only $\approx 0.8\ M_\odot$ of Fe-peak elements plus some IME with expansion velocities $\gtrsim$ 10000 km/s. In contrast to the delayed detonation models IME are produced in model DET2 in initially low density layers, i.e., a deflagration stage to lower the density is not required. The kinetic energy of the ejecta of model DET2 is less than that of model DET1 due to its lower mass. Nevertheless, the *specific* kinetic energy, i.e., the mean kinetic energy per mass, is somewhat larger, because the initial binding energy of model DET2 is is smaller by a factor of $\simeq$ 2 compared to model DET1. In model DET2 the ^{56}Ni -distribution has no central hole, because the low central density inhibits neutronization, and helps to avoid an overproduction of neutron-reach isotopes like e.g., ^{54}Fe, which are typical for models with a higher central density.

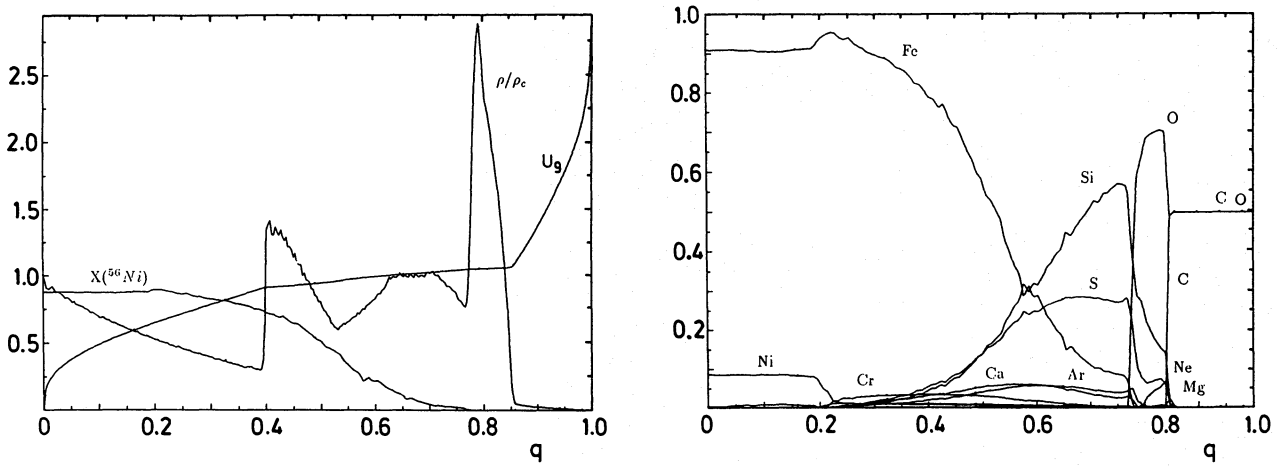

Fig. 8. Same as Fig. 1 but for model DET2ENV2

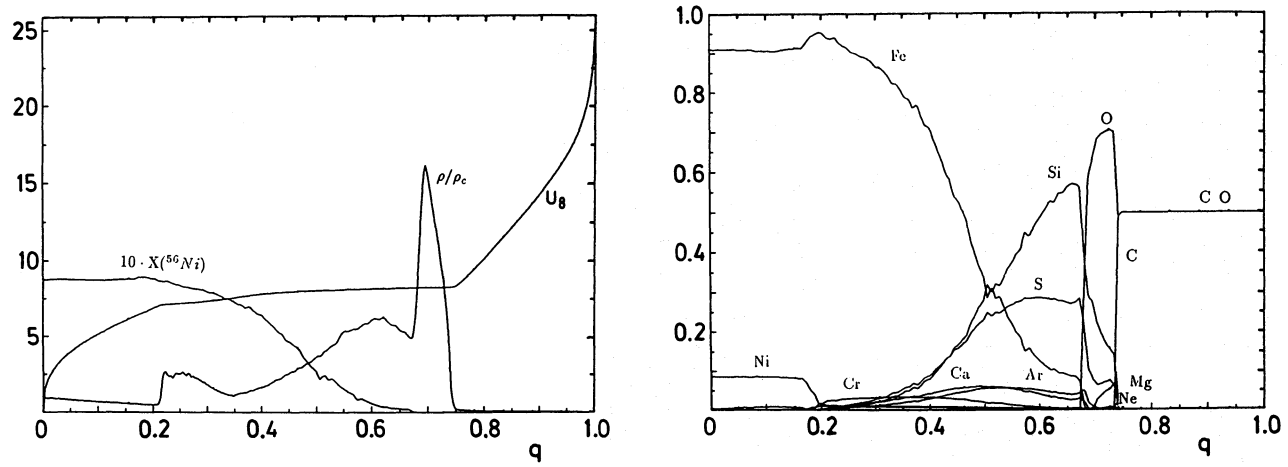

Fig. 9. Same as Fig. 1 but for model DET2ENV4 and the velocity given in units of 10^8 cm/s

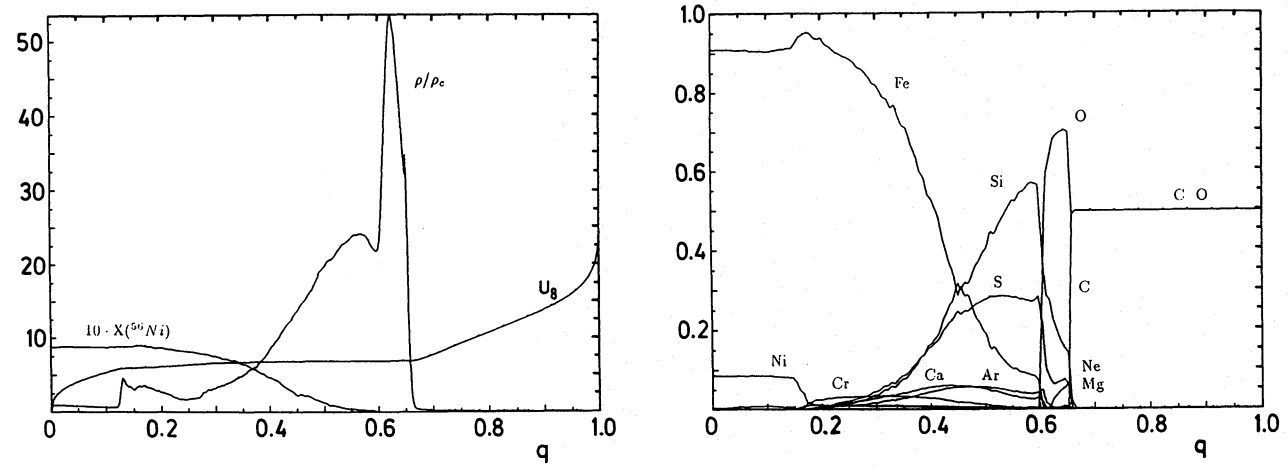

Fig. 10. Same as Fig. 1 but for model DET2ENV6 and the velocity given in units of 10^8 cm/s

The models with an envelope mass between 0.2 and 0.6 $M_\odot$ (Figs. 8-10) show a hydrodynamical behaviour similar to the pulsating delayed detonation model PDD3. Again, the outgoing detonation/shock wave collides with a low density envelope and an inward moving shock is formed which causes a strong deceleration of burnt material. Obviously, the deceleration of matter is increasing with increasing mass of the envelope and the resulting dense mass shell becomes more pronounced (Figs. 8-10).

We want to point out that, similar to model PDD3, the interaction region of the shock wave with the extended envelope are characterized by large density and pressure gradients of opposite sign, i.e., those regions are Rayleigh-Taylor unstable (Khokhlov et al. 1991). Thus, mixing processes may occur similar to those implied by observations and multi-dimensional simulations of SN1987A (see e.g., Müller et al. 1991b; and references therein).

3. Light curves

Bolometric and monochromatic LCs have been calculated for the SN Ia models discussed in the previous section. In spite of its shortcomings (see Sect. 2.3) we have also included model W7 of Nomoto et al. (1984) in our investigation, because it has been widely used in the past. A detailed description of our LC model can be found in found in H1 and H2. Its main features are:

a) A LTE radiation transfer scheme (including an energy equation for both matter and radiation) which is based on the time-dependent radiation moment equations. The equations are discretized in implicit form and allow for a consistent treatment of scattering effects.
b) A detailed equation of state with an elaborated treatment of the ionization balance and the ionization energy.
c) Time-dependent expansion opacities, which are tabulated as a function of density, temperature, expansion rate and chemical composition (see H2). The composition mixtures used represent certain burning stages (Table 3). Because, in different explosion models the ejecta contain layers of similar composition, the opacity can be interpolated rather well by using a relatively small set of tables (see Table 4).
d) Usage of Rosseland as well as Planck mean opacities, because they can differ by more than an order of magnitude (see H2).
d) Inclusion of Thomson scattering and line scattering (in a two-level approach) which enter the Planck mean opacity. In extension to H2 line scattering is treated in a frequency dependent two-level approximation. The respective equations are given in H2 (see Eqs. 30 and 32).
e) A Monte-Carlo gamma-ray transport scheme taking into account all relevant gamma transitions and interaction processes (see H1).
f) Homologously expanding background models, because homology is established in SNe Ia within less than an hour (H2). Thus, the hydrodynamic equations are not solved explicitly as e.g., required in our SN II LC project (see Müller & Höflich 1991).

3.1. Structure of the ejecta

In Figs. 11-15 the Rosseland mean opacity χ_R, the corresponding optical depth τ_R, the temperature T and the density ρ of the ejecta are given as a function of distance r for models N32, DF1, PDD3 and DET2ENV2, respectively.

The delayed detonation model N32 (Figs. 11-12) is a representative case of all models without an envelope or pulsation. Its density shows an overall monotonic decrease with distance. Note in this respect that the non-monotonic features present in

Table 3. Composition mixtures for which opacity tables have been calculated. The columns give the logarithms of the mass fractions of the various chemical elements.

Table:	1	2	3	4	5	6	7	8
He	-1.82	-13.42	-11.34	-10.15	-10.10	-9.85	-9.86	-6.97
C	-5.19	-7.53	-6.19	-5.57	-2.98	-8.40	-0.39	-1.08
O	-7.45	-6.72	-5.44	-4.55	-0.16	-7.47	-0.29	-1.08
Ne	-7.47	-11.05	-9.86	-8.09	-3.89	-11.80	-1.22	-2.40
Na	-10.92	-11.81	-9.40	-7.90	-4.48	-13.09	-2.14	-3.76
Mg	-7.30	-6.67	-5.37	-4.78	-1.19	-7.29	-1.98	-2.76
Si	-6.50	-1.48	-0.52	-0.24	-0.82	-1.93	-3.11	-2.98
P	-5.67	-6.45	-5.82	-5.77	-2.56	-7.03	-3.48	-4.48
S	-5.87	-1.37	-0.62	-0.55	-1.16	-1.76	-3.96	-4.65
Cl	-6.35	-6.21	-5.45	-5.00	-3.59	-6.56	-5.36	-5.12
Ar	-5.27	-1.79	-1.24	-1.38	-2.16	-2.13	-3.93	-4.41
K	-5.99	-6.19	-5.54	-5.13	-4.83	-6.49	-4.09	-5.96
Ca	-4.36	-1.55	-1.21	-1.56	-3.72	-1.84	-4.46	-2.93
Sc	-7.11	-6.71	-6.37	-6.40	-6.06	-6.99	-5.75	-6.26
Ti	-4.32	-2.86	-2.91	-3.70	-4.05	-3.05	-5.23	-4.08
V	-7.38	-3.86	-3.79	-4.03	-4.54	-3.94	-8.97	-4.27
Cr	-4.15	-1.44	-1.70	-2.48	-4.19	-1.53	-5.13	-1.84
Mn	-6.24	-2.03	-2.20	-2.69	-5.53	-1.98	-5.32	-1.87
Fe	-0.04	-0.08	-0.51	-1.14	-3.51	-0.05	-3.57	-0.23
Co	-3.09	-6.17	-6.10	-5.71	-3.35	-6.02	-3.69	-3.07
Ni	-1.11	-2.18	-2.34	-2.47	-3.20	-2.03	-3.02	-1.01

Table 4. Opacity tables used for the LC calculations of the various explosion models. The table entries give the numbers of the opacity tables (as defined in Tab. 3) and their corresponding mass coordinates. In order to obtain the opacity for a given mass coordinate one has to interpolate between the respective opacity tables. For mass coordinates smaller (larger) than the smallest (largest) mass coordinate given as a table entry no interpolation is performed. For example, the opacity for model N21 at $m(r) = 0.50 M_*$ is interpolated using opacity tables #1 and #2, while the opacity for model N32 at $m(r) = 0.95 M_*$ is given directly by opacity table #5.

DET1	1 / 0.96	2 / 0.97	3 / 0.98	4 / 0.99		
DF1	1 / 0.12	3 / 0.73	3 / 0.77	5 / 0.78	7 / 0.81	
DF1MIX	8 / 1.00					
W7	1 / 0.55	2 / 0.60	3 / 0.66	4 / 0.76	5 / 0.83	7 / 0.92
N21	1 / 0.47	2 / 0.68	3 / 0.83	4 / 0.93	5 / 0.98	
N32	1 / 0.20	6 / 0.32	3 / 0.68	4 / 0.90	5 / 0.93	
PDD3	1 / 0.30	2 / 0.50	3 / 0.68	4 / 0.82	5 / 0.86	7 / 0.88
DET2	1 / 0.35	2 / 0.54	3 / 0.68	4 / 0.90	5 / 0.93	
DET2ENV2	1 / 0.30	2 / 0.46	3 / 0.58	4 / 0.77	5 / 0.80	7 / 0.86
DET2ENV4	1 / 0.26	2 / 0.41	3 / 0.51	4 / 0.68	5 / 0.70	7 / 0.75
DET2ENV6	1 / 0.23	2 / 0.36	3 / 0.45	4 / 0.60	5 / 0.62	7 / 0.67

the density distribution are a result of the numerical treatment of burning during the explosion (see Sect. 2.4) which, however, do not significantly hamper our LC results. At day 15, the opacity is slowly varying in the range 0.04 cm^2/g$\lesssim \chi_R \lesssim$ 0.13 cm^2/g, which together with the density structure results into a smoothly decreasing optical depth as a function of distance. Thus, an extended photosphere is formed. As a consequence, the temperature is slowly decreasing with distance in the outer layers. Near the center the temperature gradient becomes flat, because of a lack of gamma photons from the central hole in the ^{56}Ni - distribution (see also H1) and because the diffusion time scale, which can be approximated by

$$t_{diff} \approx \frac{\Delta r \, \Delta \tau}{c} \quad , \tag{2}$$

is still large ($\approx$ 10 days). Here, Δr, $\Delta \tau$ and c are the distance between two points in the ejecta, the corresponding optical depth difference, and the velocity of light, respectively. At a later epoch (e.g., at day 50; see Fig. 12) the mean opacity has become smaller ($\approx$ 0.03 cm^2/g), because of the lower temperature of the ejecta. At this epoch, the ejecta are almost transparent and a nearly isothermal structure is established.

A qualitatively similar structure and evolution is obtained for the other delayed detonation, deflagration and detonation models. However, several quantitative differences are found, which are largest for the deflagration model DF1 (Fig. 13). Because of its lower kinetic energy, the expansion rate for the bulk of the ejecta is somewhat slower. Consequently, at a given epoch density and optical depth are larger throughout the ejecta, i.e., the

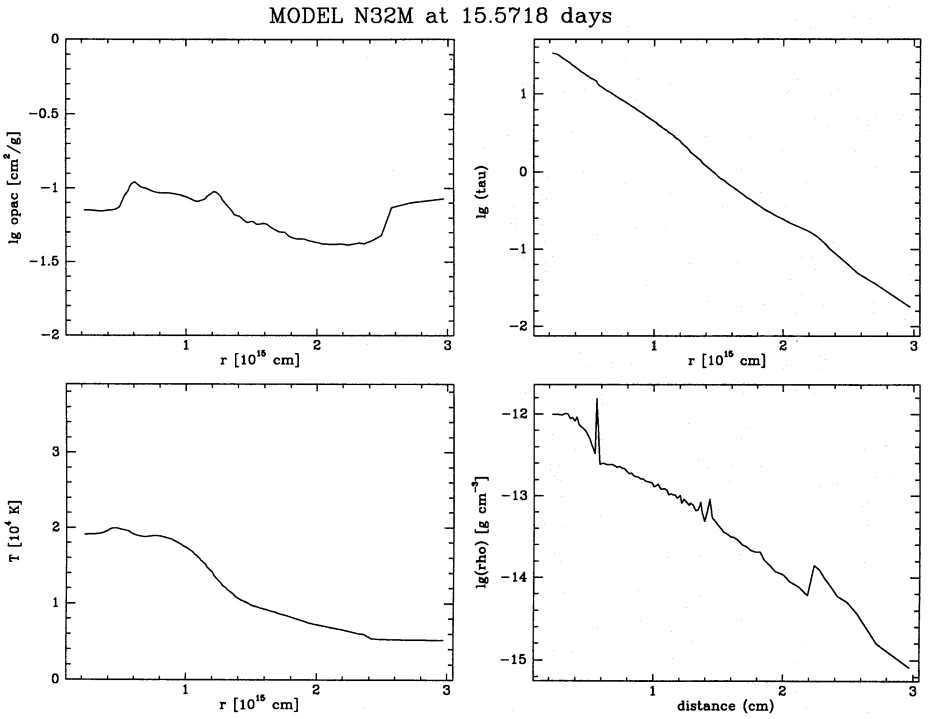

Fig. 11. Rosseland mean opacity χ_R (top left), corresponding optical depth τ_R (top right), temperature T (bottom left) and density ρ (bottom right) as a function of distance for the delayed detonation model N32 at day 15

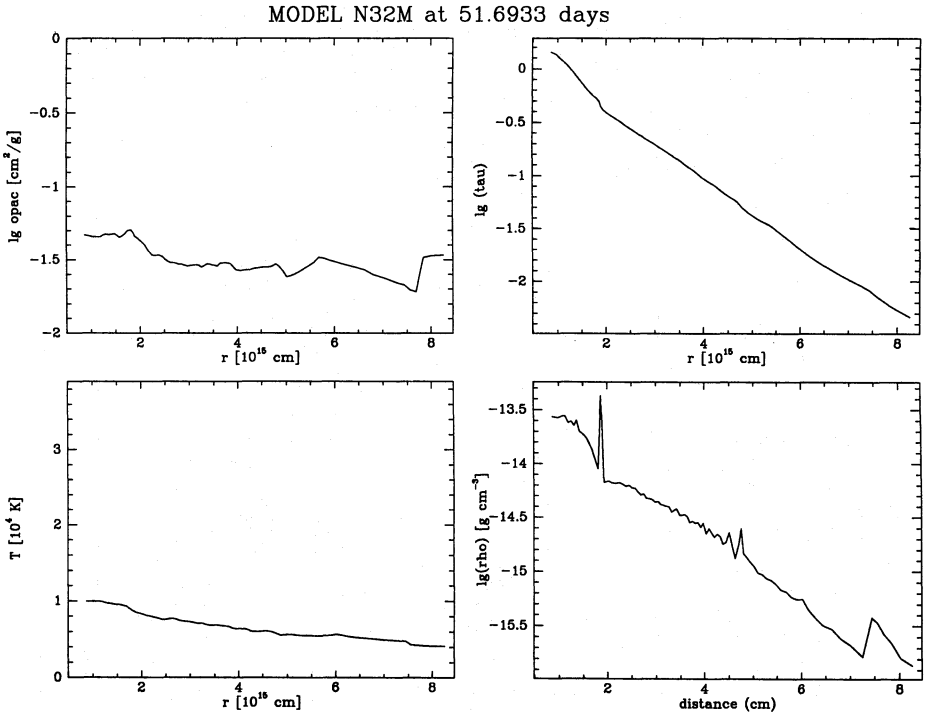

Fig. 12. Same as Fig. 11 but at day 52

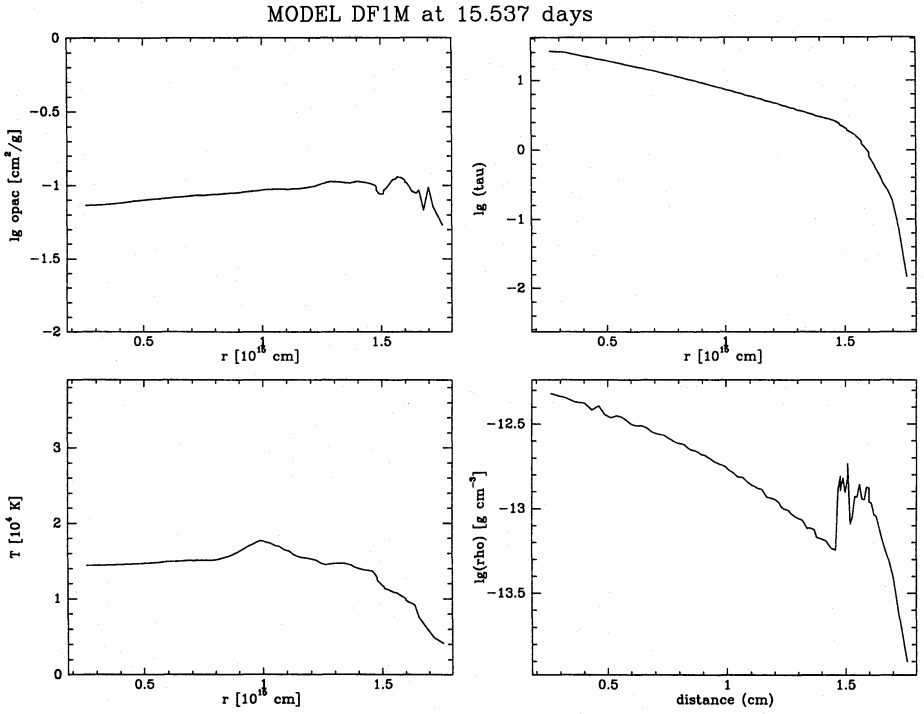

Fig. 13. Same as Fig. 11 but for model DF1

photosphere is located closer to the outer edge of the ejecta. In model DF1 the temperature profile is decreasing near the center due to the huge hole in the ^{56}Ni -distribution.

The structure of the ejecta is very different in model PDD3 and in all envelope models (Figs. 14 and 15). The density structure of model PDD3 shows an inner region of relatively high density and a pronounced density maximum with a sharp outer edge located where the interaction between the inward propagating shock wave and the expanding central parts occured during the explosion (see Sect. 2.5). A similar structure is present in the density profiles of all envelope models due to the interaction of the ejecta with the extended envelope. The temperature profiles of model PDD3 and of the envelope models are quite similar, because in all these models the optical depth is rapidly changing across the narrow dense shell implying a very sharp photosphere with a large temperature gradient. Both below and above the photosphere an almost isothermal temperature region is established. In the envelope models the isothermal central re-

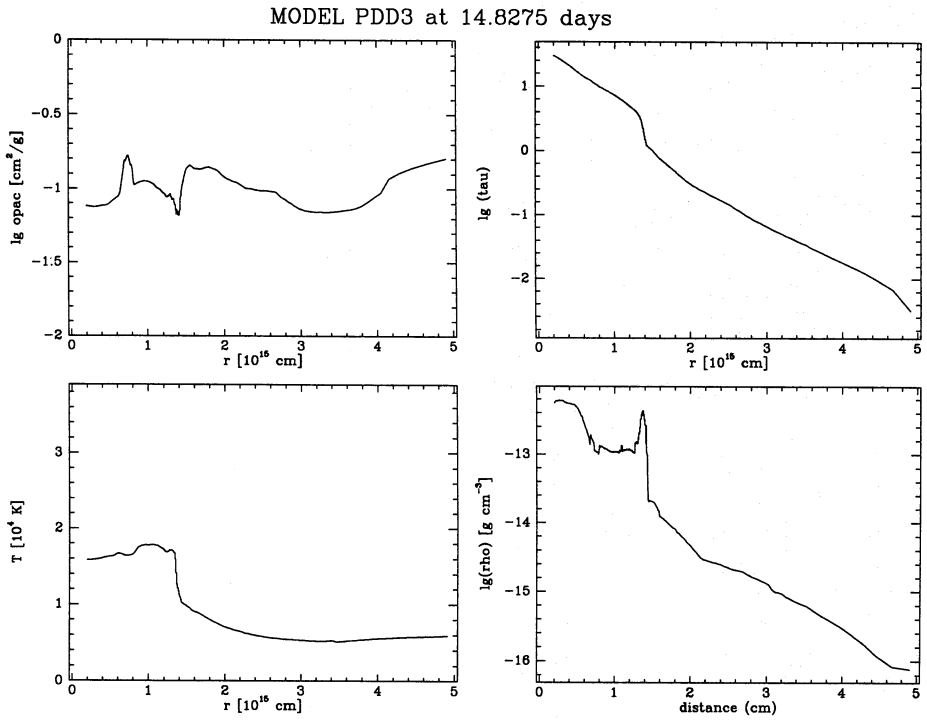

Fig. 14. Same as Fig. 11 but for model PDD3

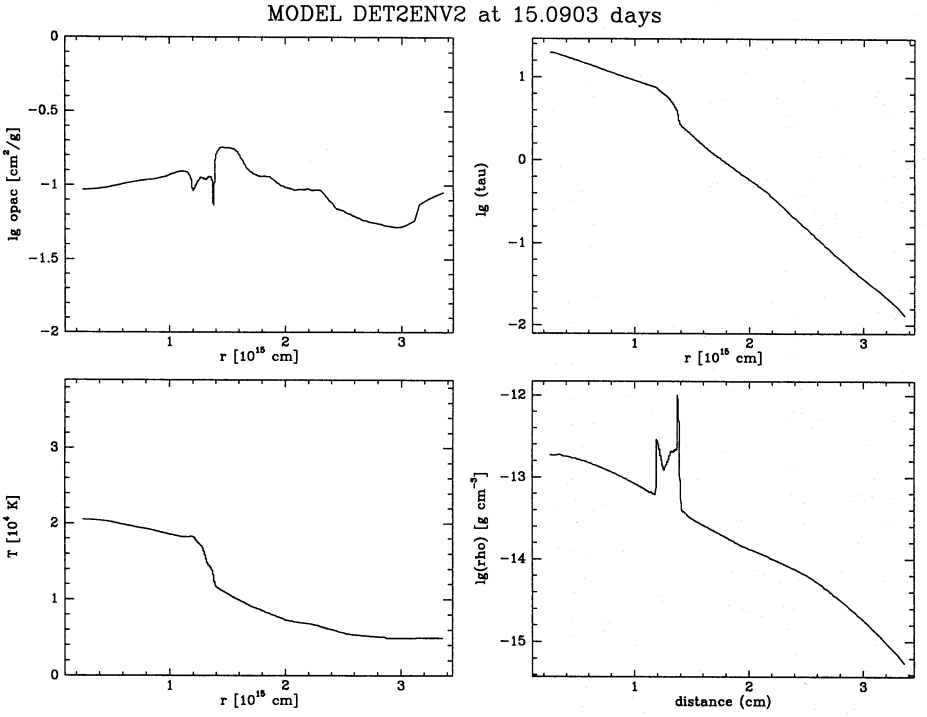

Fig. 15. Same as Fig. 11 but for model DET2ENV2

gion is not caused by the (hole in the) ^{56}Ni -distribution but by radiation which is trapped inside the optically thick shell (see also Fig. 8-10).

3.2. Photospheric velocity

The velocity of the photosphere v_{ph} can be measured approximately by the Doppler shift of spectral lines without invoking a detailed spectral analysis. Figs. 16-18 show $v_{ph}(t)$ as a function of time for our models. The figures clearly demonstrate that the behaviour of v_{ph} is model dependent. In detonation and delayed detonation models $\rho(r)$ and $v(r)$ are monotonic and v_{ph} continuously decreases with time as the photosphere slowly moves inward in mass due to the geometrical dilution of matter. In the pulsating delayed detonation model and in all envelope models a dense shell of matter is present (see previous subsection)

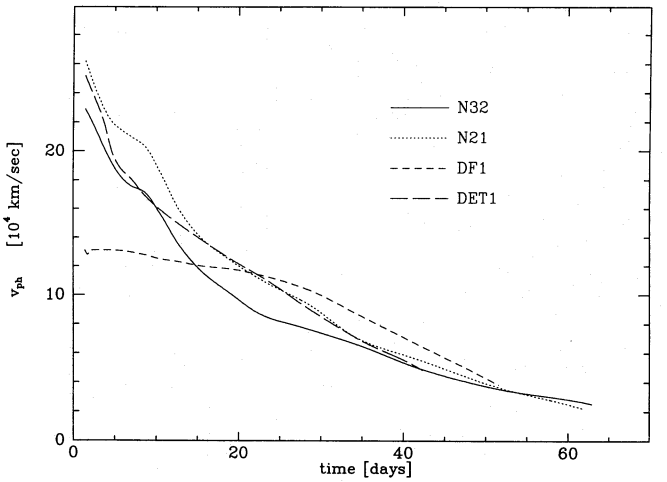

Fig. 16. Photospheric velocity v_{phot} as a function of time for models N32, N21, DF1 and DET1

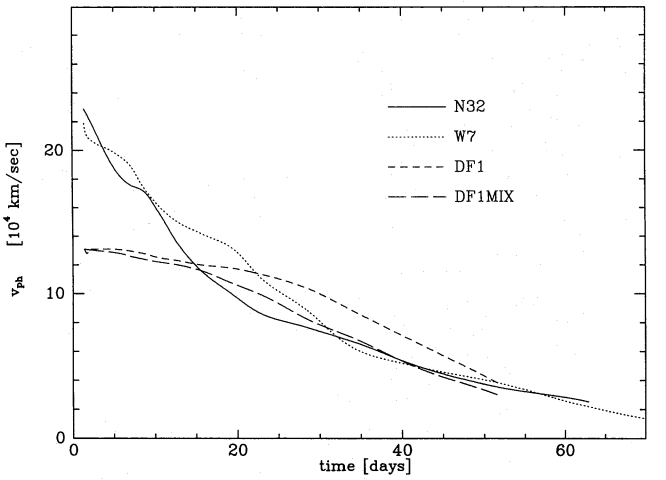

Fig. 17. Same as Fig. 16 but for models N32, W7, DF1 and DF1MIX

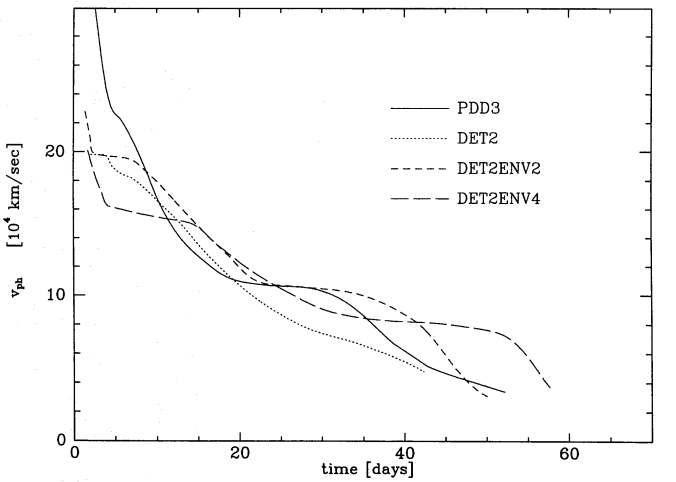

Fig. 18. Same as Fig. 16 but for models PDD3, DET2, DET2ENV2 and DET2ENV4

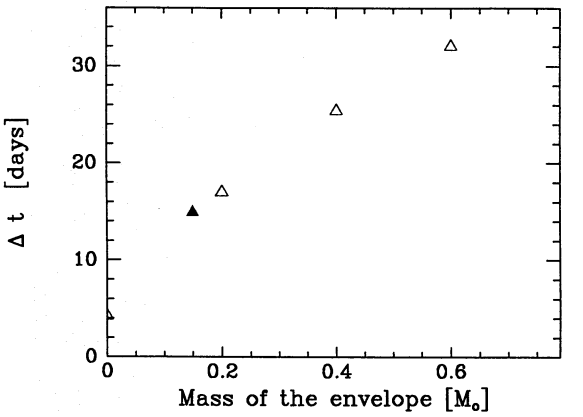

Fig. 19. Duration of the plateau in the photospheric velocity (defined by $\Delta v_{phot} \leq 2000$ km/s) as a function of envelope mass for models PDD3, DET2ENV2, DET2ENV4 and DET2ENV6 (see Table 5)

the material velocity inside the shell being almost constant. The photosphere stays inside this shell for some time giving rise to a plateau in $v_{phot}(t)$ after maximum light (see Figs. 16-18). Note that there exists a second plateau in the photospheric velocity *before* maximum, which in some models (e.g., model N32) is only visible as a shoulder. This pre-maximum plateau can be explained as follows. In all models (except the deflagration models) the expansion velocity $v(m)$ rapidly drops in the outermost mass layers (see Figs. 1-11), and thus even a slight retreat (in mass) of the photosphere causes a large decrease of v_{phot}. Further inward from the surface $v(m)$ changes less rapidly. This fact and the still large optical depth of the respective mass layers produce the pre-maximum plateau of v_{phot}, which is more or less pronounced depending on the overall expansion rate of the explosion model (see Figs. 16-18). Afterwards v_{phot} begins to decrease again when the diffusion dominated regime is encountered which happens near maximum light.

Before maximum light all models except models DF1 and DF1MIX show a fast variation of v_{phot}, because of strong variations of the matter velocity in the outer layers of the ejecta from, say, $\sim$ $(2-3)$ 10^4 km/s down to 10^4 km/s. In the deflagration models, in contrast, there is almost no fast moving matter and therefore the photospheric velocity shows a plateau before maximum and monotonically decreases after maximum as in the models without an envelope. We thus see that the deflagration, detonation and delayed detonation models can be discriminated from models with an envelope quite easily on the basis of the behaviour of photospheric velocity after maximum light. For the models with an envelope the duration t_{plat} of the plateau gives a measure of the envelope mass. Fig. 19 clearly shows that t_{plat} is almost linearly related with the envelope mass of models PDD3, DET2ENV2, DET2ENV4 and DET2ENV6.

The photospheric velocities at maximum light are ranging from 8000 to 17000 km/sec for our models (see Table 5). This observational quantity can also be used for a model discrimination. There is, however, no unique correlation between v_{phot} and M_{Ni} or $< v >$, e.g., because the location of the photosphere depends on such factors as the expansion rate, the density structure,

the location of the radioactive ^{56}Ni which influences the temperature and therefore the opacity of matter, etc. The influence of the ^{56}Ni -distribution becomes especially obvious from a comparison of the deflagration models DF1MIX and DF1 (Fig. 17) which differ only in the radial distribution of the chemical elements, and of ^{56}Ni in particular. The mixed model shows a significantly stronger decrease of the photospheric radius, because the enhanced escape probability for gamma-ray photons causes a smaller total energy deposition and, consequently, a lower temperature and opacity.

3.3. Bolometric light curves

The bolometric LCs of our models are shown in Figs. 20-22 and some characteristic LC quantities are given in Table 5. The bolometric LCs rise to maximum light within 7 to 20 days and all show a broad maximum. As demonstrated in H2 the early evolution of the LC depends on: (i) the expansion rate which determines the column density and thus the diffusion time scale; (ii) the energy release due to the radioactive decay of ^{56}Ni and ^{56}Co ; (iii) the distribution of ^{56}Ni and ^{56}Co inside the ejecta; and (iv) on the total mass and the density distribution of the ejecta. After about 30 to 80 days the ejecta become transparent, i.e., the shape of the bolometric LC is mainly determined by the amount of energy deposited by the radioactive decay of ^{56}Co (H1). Consequently, the slopes of the light curves are similar at late epochs the actual slope mainly depending on the initial ^{56}Ni -distribution and the expansion rate of the matter (H1). As light curves can be distinguished best by their rise time and their shape near maximum our discussion below will be focused on these phases.

Reliable theoretical calculations of the early LC require an appropriate treatment of the relevant physics (see H2). Several

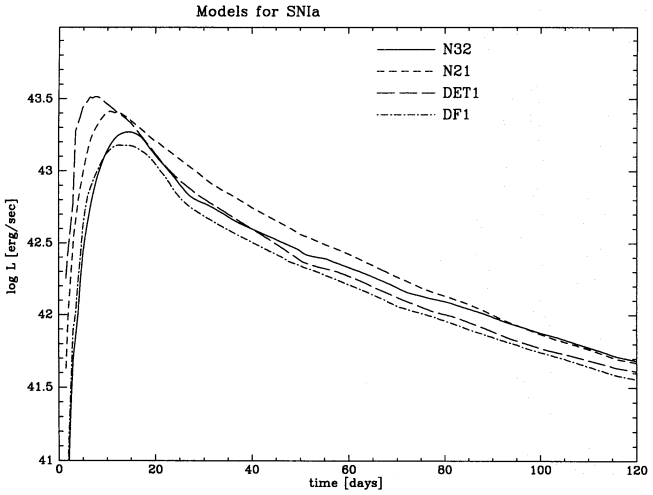

Fig. 20. Bolometric light curves as a function of time for the models N21, N32, DF1 and DET1

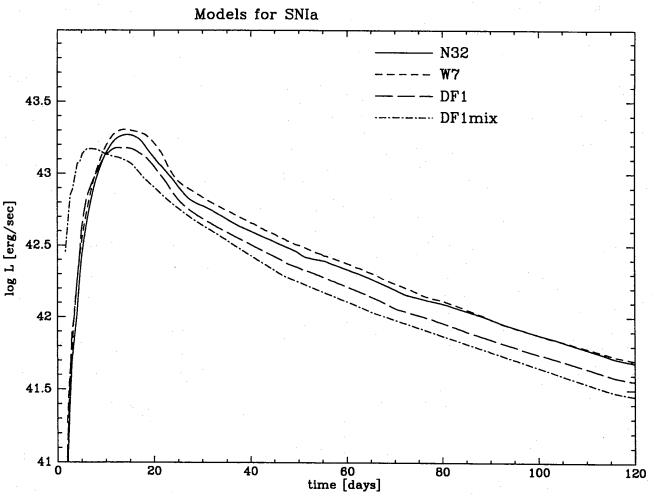

Fig. 21. Bolometric light curves as a function of time for the models N32, W7, DF1, DF1mix

Table 5. Some characteristics of the investigated SN Ia explosion models. The quantities given in columns 2 to 11 are: The maximum bolometric luminosity L_{bol} in ergs/s, the rise time to bolometric maximum t_{bol} in days, the total energy deposition rate inside the ejecta at bolometric maximum $Q_\gamma(t_{bol})$ in ergs/s, the absolute visual magnitude M_V, the rise time to visual maximum t_V in days, the absolute blue magnitude M_B, the rise time to blue maximum t_B in days, $(B-V)$ at visual maximum, the ratio of the bolometric and gamma-ray luminosity at the time of bolometric maximum A_{bol} and at the time of visual maximum A_V.

Model	lg L_{bol}	t_{bol}	lg $Q_\gamma(t_{bol})$	M_V	t_V	M_B	t_B	$(B-V)$	A_{bol}	A_V	Symbol
DET1	43.51	7.5	43.53	-19.99	8.5	-20.04	8.0	-0.04	0.96	1.04	⋆
DF1	43.18	13.5	43.09	-19.38	15.5	-19.22	14.5	0.16	1.23	1.38	○
DF1MIX	43.17	7.3	43.30	-19.17	13.2	-19.10	8.1	0.13	0.75	1.08	○
W7	43.30	14.0	43.18	-19.66	15.5	-19.48	14.0	0.19	1.31	1.43	○
N21	43.41	10.7	43.41	-19.80	12.7	-19.71	11.3	0.09	1.01	1.14	●
N32	43.27	14.5	43.11	-19.56	15.2	-19.39	14.5	0.16	1.42	1.48	●
PDD3	43.28	15.0	43.16	-19.45	15.9	-19.32	16.0	0.14	1.33	1.34	▲
DET2	43.32	13.7	43.18	-19.67	14.2	-19.52	13.7	0.15	1.39	1.42	△
DET2ENV2	43.27	16.6	43.13	-19.41	19.5	-19.40	16.8	0.17	1.31	1.49	△
DET2ENV4	43.25	19.0	43.10	-19.31	21.4	-19.34	19.3	0.22	1.41	1.44	△
DET2ENV6	43.21	19.3:	43.09	-19.21	21.8	-19.14	19.8:	0.24	1.26	1.32	△

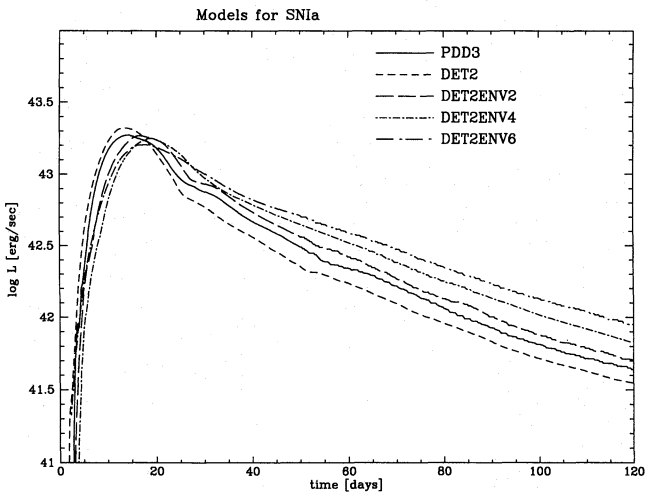

Fig. 22. Bolometric light curves as a function of time for the models PDD3, DET2, DET2ENV2, DET2ENV4, DET2ENV6

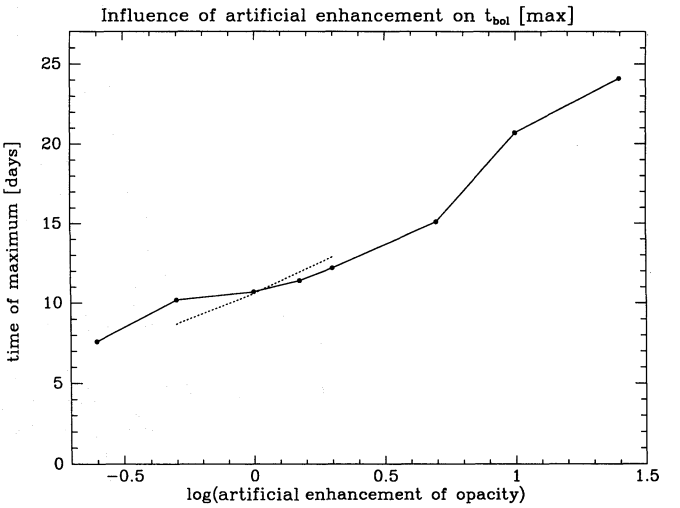

Fig. 23. Rise time to bolometric maximum t_{bol} as a function of the artificial opacity enhancement factor C_{art} for model N21. The solid line shows our result, while the dotted line is obtained when a spatially constant opacity is used (from H2)

groups have shown that the light curves of SNe Ia can be fitted by artificially adjusting the time-dependent opacity, which is assumed to be *constant in space* (Shigeyama et al. 1992). This procedure is absolutely impossible, however, if a realistic temperature dependent opacity is used (see H2). In fact, the results become almost independent of the actual value of the opacity (provided a realistic one is used), because the most important factor determining the shape of the LC is the rapid decrease of the opacity at temperatures below $\approx 2\ 10^4$ K.

3.3.1. Influence of the opacity

There are several uncertainties related with the calculation of the opacity, namely, errors in the individual oscillator strengths of the used transitions and "missing lines". In addition, the opacity is calculated in a local approximation, i.e., the occupation numbers are given assuming local thermodynamical equilibrium (LTE) and the expansion effects are calculated under the assumption that density, temperature and velocity gradient do not vary over the mean free path of a photon. For our opacity calculations about 530000 line transitions are taken into account based on the compilation of Kurucz (1989). Although being quite large, this line list may nevertheless be incomplete. We find that decreasing the number of transitions from $5\ 10^5$ to $5\ 10^4$ reduces the opacity by a factor of $\lesssim 1.5$. However, according to the classical sum rule and tests with up to $3\ 10^6$ transitions the opacity will increase by $\approx 10\%$, if more than $5\ 10^5$ transitions are taken into account.

In order to check for possible effects of uncertainties in the opacity, we have tested the influence of a variation of the opacity on the rise time to bolometric maximum using the delayed detonation model N21. For this purpose we multiplied the opacity by a constant factor, i.e., we assumed that the relative variation of the opacity for a given temperature, density and velocity gradient does not change. This treatment can be justified, because (to first order) the opacity scales with the sum of the oscillator strengths of the lines, and the actual ionization balance (for

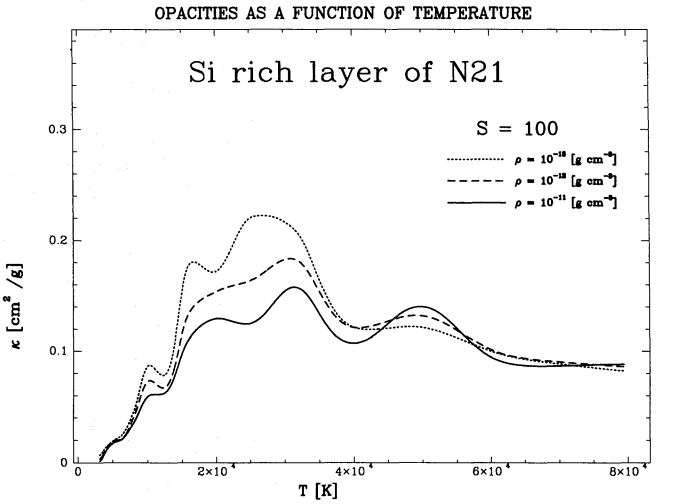

Fig. 24. Rosseland mean opacity as a function of temperature for the Si-rich layer of model N21 for different densities and an expansion rate $s = 100$ (for the precise definition of s see H2)

LTE) only depends on density and temperature, which are consistently calculated in our models.

The change of the rise time to bolometric maximum t_{bol} as a function of the artificial opacity enhancement factor C_{art} is shown Fig. 23. For comparison, we also give the results for a spatially constant opacity (taken from H2). One sees that the dependence of t_{bol} on C_{art} is remarkably weak for $0.3 \lesssim C_{art} \lesssim 3$. Within this range of C_{art} the rise time changes only by $\simeq \pm 1$ day, i.e., in the range of a "realistic" opacity (see above). For smaller enhancement factors C_{art} the rise time decreases more rapidly, whereas it rapidly increases for $C_{art} \gtrsim 5$. Such a behaviour of t_{bol} can be understood as follows.

The realistic opacity used in our computations is strongly varying with temperature and density. During the first few weeks

after the explosion $-14 \lesssim \lg \rho \lesssim -11$ and the expansion rate is typically in the range of $1 \lesssim \lg s \lesssim 3$. In this parameter range the opacity rapidly becomes small when the temperature drops from $T \gtrsim 2\ 10^4$ K to $T \lesssim 10^4$ K (see Figs. 3 and 4 in H2). For temperatures $\gtrsim 2\ 10^4$ K the opacity typically is of the order of $\simeq 0.1$ cm^2/g, but when the temperature decreases below a critical temperature $T_{cr} \simeq 10^4$ K the opacity drops to values of $\simeq 10^{-2} - 10^{-3}$ cm^2/g (see Fig. 24). For semi-transparent layers a negative feedback between matter and radiation exists. Radiative heating of these layers increases (decreases) when the opacity decreases (increases), i.e., the photosphere stays hotter. This self-balancing, which was already discussed in detail in our previous paper (H2), prevents the formation of a rapidly inward propagating cooling wave. Thus the inner part of the ejecta remain opaque and the diffusion time scale remains much larger than the expansion time scale (see Eq. 2), i.e., the evolution of the ejecta is determined by adiabatic cooling and local radioactive heating.

Consider the evolution of a mass element inside the expanding ejecta assuming no radiation transport. During the first few weeks the ejecta are radiation dominated and the energy balance is given by

$$\frac{4\,aT^3}{\rho}\frac{dT}{dt} - \frac{4aT^4}{3\rho^2}\frac{d\rho}{dt} = \dot{q}_{Ni}\,, \qquad (3)$$

where $\dot{q}_{Ni} \simeq 3.9\ 10^{10} \exp(-t/\tau_{Ni})$ ergs/g/s is the energy deposition rate, $\tau_{Ni} = 8.8$ days is the ^{56}Ni decay time. We neglect the contribution of ^{56}Co , because ^{56}Ni dominates the energy input during the first $\simeq 1 - 2$ weeks. For a freely expanding envelope $\rho = \rho_0\,(t_0/t)^3$. Thus, one obtains from Eq. (3)

$$\frac{d\ln T}{dt} = -\frac{1}{t} + \frac{\rho\,\dot{q}_{Ni}}{4\,a\,T^4}\,. \qquad (4)$$

A stationary solution of Eq. (4) gives (a first-order approximation of) the temperature inside a mass element as a function of time

$$T = \left(\frac{t\,\rho\,\dot{q}_{Ni}}{4\,a}\right)^{1/4}\,. \qquad (5)$$

From Eq. (3) we can determine a critical time t_{cr} at which the temperature drops below the critical temperature T_{cr} discussed above by simply equating the right hand side of Eq. (3) to T_{cr}. Of course this moment will be different for different mass elements. This will happen first in the outermost layers of the ejecta, whereas in the center the critical temperature will be encountered last. We can roughly estimate a typical value of t_{cr} by substituting the density in Eq. (4) by the mean density of the ejecta, which is given by the mean expansion velocity of the ejecta as $\langle\rho\rangle = 4\,M_*/3\pi\langle v\rangle^3\,t^3$. Then we obtain

$$t_{cr}\ \exp\left(\frac{t_{cr}}{2\,\tau_{Ni}}\right) = \frac{10\ \text{days}}{\langle v_9\rangle^{3/2}}\left(\frac{M_*}{M_\odot}\right)^{1/2}\left(\frac{10^4\text{K}}{T_{cr}}\right)^2\,, \qquad (6)$$

where v_9 is the velocity in units of 10^9 cm/s. For typical values of $\langle v_9\rangle \simeq 0.8 - 1.0$ (see Table 5) one finds $t_{cr} \simeq 7 - 13$ days. At this time radiation transport effects become important for a significant fraction of the ejecta. Note that for models with an envelope or which undergo a large scale pulsation (like model PDD3), $< v_9 >$ should be substituted by the expansion velocity of the dense shell, because the outermost layers dominate the averaging of $< v_9 >$ but have little effect on the diffusion time scale. It is obvious that as soon as T_{cr} is reached for most of the ejecta, there exists no mechanism to further trap the radiation and to postpone the formation of a bolometric maximum.

For $C_{art} \lesssim 0.3$ the opacity is reduced to values of about 0.02 cm^2/g implying that large parts of the ejecta become transparent early on and radiative cooling can take place. For moderate enhancement factors C_{art} the balance between adiabatic cooling and gamma-ray energy input determines the epoch when the local temperature drops below 12000 to 20000 K. Then, suddenly the envelope becomes partially transparent. Because the opacity is strongly decreasing with temperature, a change in χ has only very little influence on the timing. For large C_{art} the diffusion time scale is kept large for the layers containing ^{56}Ni , because even at 5000 K the opacity exceeds 0.2 cm^2/g, i.e., the diffusion time scale remains larger than the expansion time scale long after maximum light and, consequently, the "temperature" effect does not work.

In conclusion, even taking into account uncertainties in the opacity, the rise time to bolometric maximum t_{bol} is a weak function of the actual size of the opacity, because it is mainly determined by the variation of the opacity with the local temperature.

3.3.2. Standard models

First we want to discuss models without envelopes, namely the detonation model DET1, the low density detonation model DET2, the delayed detonation models N21 and N32, the deflagration models DF1 and DF1MIX, and deflagration model W7 of Nomoto et al. (1984).

The influence of the average expansion velocity $< v >$ on the bolometric LC is obvious from Fig. 25a, which shows the rise time to bolometric maximum t_{bol} as a function of $< v >$. Models DET1, N21, N32 and W7 form a sequence in which the specific kinetic energy is gradually decreasing from model DET1 to model DF1. In addition, the outer edge of the ^{56}Ni -distribution is gradually shifting towards the center. Both effects act in accordance, i.e., for all models t_{bol} decreases with increasing $< v >$. For the detonation model DET1, where $< v > \simeq 1.01\ 10^9$ cm/s, the rise time is $\simeq 10$ days. The latter increases to $\simeq 14.5$ days for the delayed detonation model N32, where $< v > \simeq 8.9\ 10^8$ cm/s.

As models DET1, N21 and N32 have the same mass (1.4 $M_\odot$), their different specific kinetic energies are due to differences in the flame propagation during the explosion. Therefore, $< v >$ correlates with the amount of produced ^{56}Ni (Table 1), and consequently the ^{56}Ni -mass M_{Ni} (anti) correlates with t_{bol} (Fig. 25b). Note that qualitatively the same relation holds between the ^{56}Ni -mass, average expansion velocity and the rise time to bolometric maximum for the gamma-ray light curves of these models (see H1).

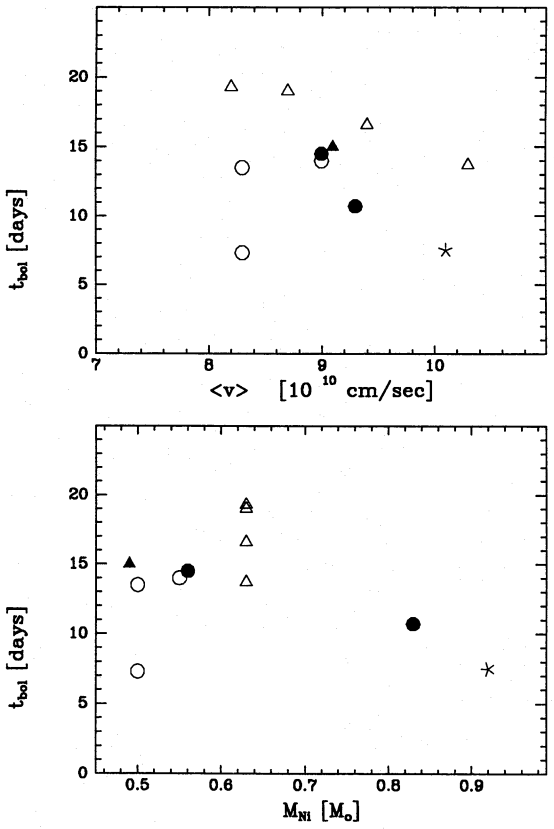

Fig. 25. Rise time to bolometric maximum t_{bol} as a function of (a; top) the average expansion velocity $< v >$, and (b; bottom) of the ^{56}Ni -mass M_{Ni} for all investigated explosion models. The different symbols correspond to the delayed detonation models N32 and N21 (•), the deflagration models DF1, DF1MIX and W7 (○), the detonation model DET1 (⋆), the pulsating delayed detonation model PDD3 (▲) and the low density detonation models DET2, DET2ENV2, DET2ENV4 and DET2ENV6 (△)

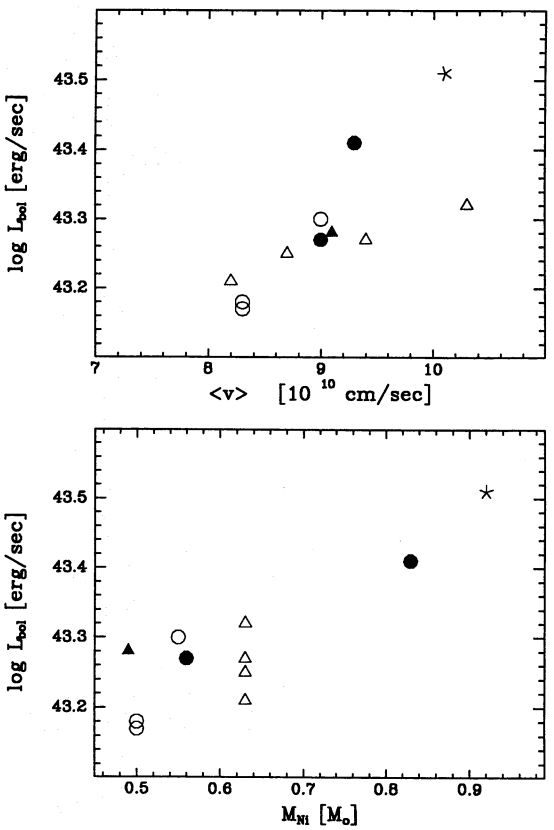

Fig. 26. Same as Fig. 25 but for the maximum bolometric luminosity L_{bol}

For the low density detonation model DET2, the white dwarf mass is smaller ($1.2\ M_\odot$) causing a smaller overall optical depth. However, this effect is somewhat compensated by the large concentration of ^{56}Ni near the center. The rise time of the detonation model DET2 is 13.7 days (as compared to $t_{bol} \simeq 10.1$ days for model DET1), although the average expansion velocity of model DET2 is larger than that of model DET1 the reason being the different ^{56}Ni -distribution. In model DET2 ^{56}Ni is concentrated near the center, whereas it is distributed throughout the star in model DET1. The effect of the ^{56}Ni -distribution is so strong that the rise time in model DET2 is even larger than that of model N21 inspide of its lower average expansion velocity.

It is not obvious that the expansion rate and the ^{56}Ni -distribution should act in the same direction. One would expect, for example, that for the deflagration model DF1, where $< v > \simeq 8.3\ 10^8$ cm/s, the rise time t_{bol} should be larger than for N32 model. However, model DF1 has a rise time of only $\simeq$ 14 days, which is less than that of model N32 where $< v >$ is larger. The reason for this behaviour is that ^{56}Ni is concentrated more towards the surface in model DF1 than in model N32 (see Fig. 2 of H1), thus partially compensating its relatively low expansion rate. The effect of the ^{56}Ni -distribution is illustrated further by the model DF1MIX in which the composition of model DF1 was completely homogenized after burning has stopped. Although artificial (as far as the process of mixing is concerned) this model represents an extreme case of a model with a *low* expansion rate and a *high* degree of mixing inside the ejecta. Because of the presence of a large amount of ^{56}Ni in the outer layers (Fig. 2 in H1) this model is characterized by a rise time almost equal to that of the detonation model DET1. Thus, mixing is a mechanism to decrease the rise time, i.e., no strict correlation can be expected between $t_{bol}, < v >$ and M_{Ni} in general.

The expansion rate also strongly influences the absolute bolometric brightness at maximum (Fig. 26a). L_{bol} is a strongly increasing function of $< v >$ for models DF1, W7, N32, DET2, N21 and DET1, because bolometric maximum is reached earlier, i.e., less ^{56}Ni has decayed at the time of maximum. For the same reason, L_{bol} is a monotonic function of the initial ^{56}Ni -mass (Fig. 26b). Although $< v >$ and M_{Ni} are not strongly correlated, both influence t_{bol} in the same direction (see above). Therefore, two directly observable quantities, namely t_{bol} and the photospheric velocity at bolometric maximum $v_{phot}(t_{bol})$ are strongly correlated with L_{bol} (Fig. 27). This allows, in principle, a determination of L_{bol} and of the visual brightness M_V (see next section) based on the measurement of the photospheric velocity at maximum light and of the time of maximum light.

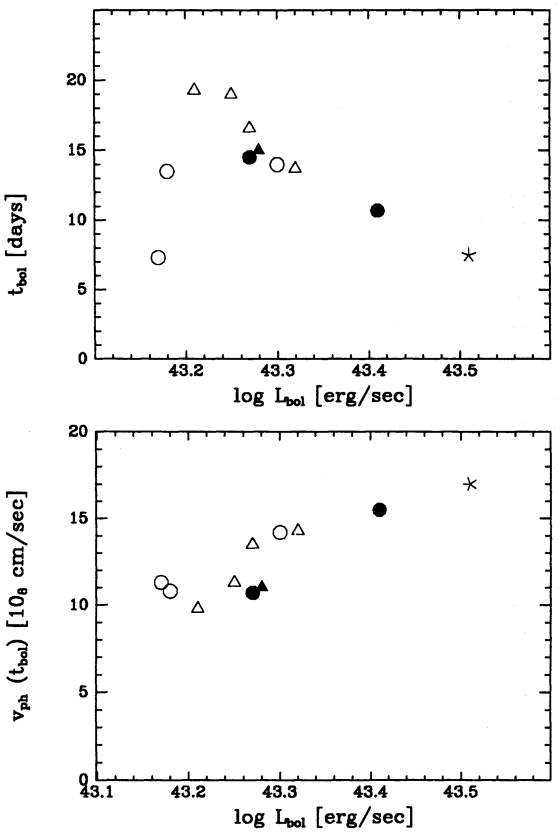

Fig. 27. Rise time to bolometric maximum t_{bol} (a; top) and photospheric velocity at bolometric maximum $v_{phot}(t_{bol})$ (b; bottom) as a function of the maximum bolometric luminosity L_{bol}. Symbols have the same meaning as in Fig. 25

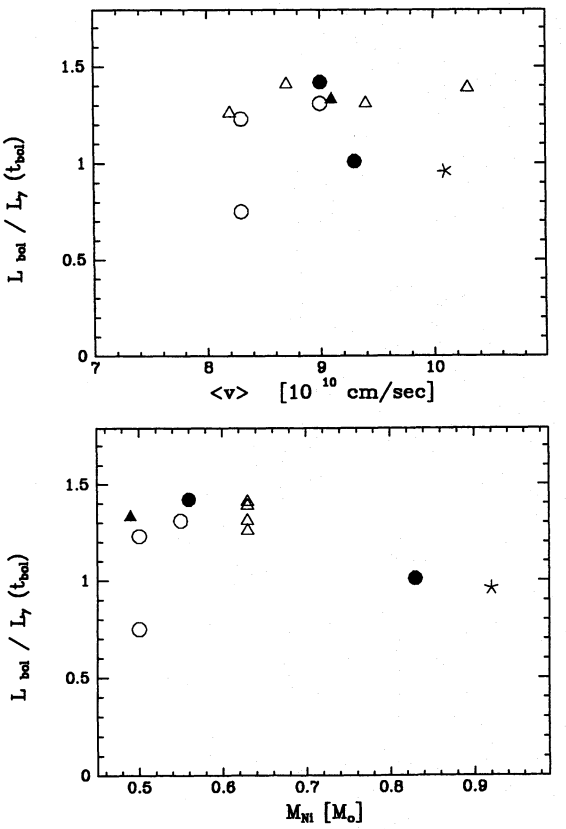

Fig. 28. Same as Fig. 25 but for the ratio of the bolometric and gamma-ray luminosity at bolometric maximum $L_{bol}/L_{\gamma})$

The "standard" deflagration models DF1 and DF1MIX again do not obey the first correlation, because in these models ^{56}Ni is produced very close to the surface. Note however, that these models can be identified (using spectral information) due to the time dependence of v_{phot} and the lack of IME at large velocities.

Finally, we want to address the question of "Arnett's law", that the luminosity at maximum is identical to the rate of energy deposition due to gamma-ray photons at the time of maximum light (Arnett et al. 1985). For a realistic (non-constant) opacity this rule does not hold. In fact, $A_{bol} \equiv L_{bol}/L_{\gamma}(t_{bol})$ lies in the range $0.75 - 1.49$ for our set of models (see Table 5). For models without mixing it is almost uncorrelated with the average expansion velocity $< v >$ and only weakly correlated to M_{Ni} (Fig. 28), because of the influence of the ^{56}Ni -distribution. However, there exists a strong correlation with t_{bol} (Fig. 29). The earlier the maximum occurs the hotter the envelope is, because the energy release per volume is decreasing with time and because the energy input rate by the radioactive decay of ^{56}Ni is larger than that of ^{56}Co due to the different decay rates (see e.g., Fig. 15 in H2). Consequently, the envelope at maximum is hotter for early maxima. This effect is also reflected by the color index (see Table 5) which provides us with a measurement of the temperature at the photosphere. The key for the understanding of this behaviour is again given by the change of the opacity as a function of temperature (see above, and Figs. 3-4

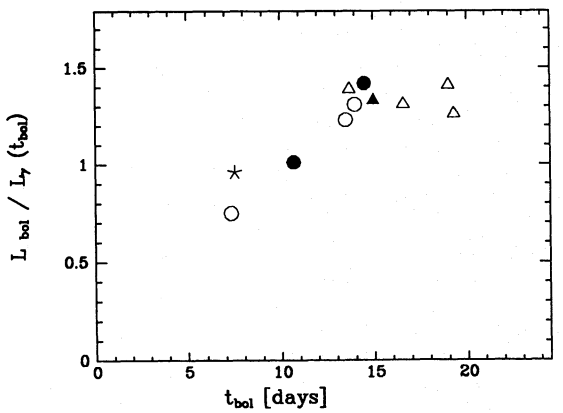

Fig. 29. Correlation between the ratio of the bolometric and gamma-ray luminosity at bolometric maximum L_{bol}/L_{γ} and the time of bolometric maximum t_{bol}. Symbols have the same meaning as in Fig. 25

of H2). In models N21 and DET1 the bulk of matter has a temperature of about 20000 K near maximum light, i.e., well above the temperature where χ strongly decreases with temperature. Consequently, A_{bol} is close to unity. However, for models with larger rise times, the photospheric region is rapidly cooled by radiation at $t \approx t_{bol}$, because a significant part of the ejecta becomes transparent, i.e., the photosphere is rapidly receding in mass. Thus, thermal energy can rapidly be released from a region which has a larger size than in the case of a constant opacity,

i.e., A_{bol} becomes much larger than unity. For the same reason, A_{bol} is much less than unity for model DF1MIX. In this model the temperature in the relevant layers is about 30000 K implying an increase of the opacity with time, i.e., less thermal energy is released than in the constant opacity case.

To maximize the rise time to maximum light one has to decrease the amount of ^{56}Ni , to concentrate it towards the center (like in model DET2), and to reduce the expansion rate (like in model DF1). However, as far as the hydrodynamics is concerned these factors are not independent of each other and the ^{56}Ni -mass is limited from observations (see, e.g., Leibundgut et al. 1991a). Our results show that for standard models, the rise times to maximum light can hardly be longer than 15 to 16 days, even if uncertainties are taken into account. So, the structure of the ejecta or the total mass must be changed to allow for slower rising supernovae.

3.3.3. Non-standard models

Now we turn to explosion models where an interaction with a low density outer envelope occurs, which can increase the rise time (see Table 5 and Fig. 22). In the delayed detonation model PDD3 such a low density envelope is created by a large scale pulsation of the white dwarf. The envelope then 'absorbs' a significant amount of the kinetic energy and decelerates the expanding inner layers of the former white dwarf (see Sect. 2.4). Although the average expansion velocity of model PDD3 is comparable with that of models N21 and N32 (Table 1) the shape of the velocity distribution of model PDD3 is very different. Model PDD3 is characterized by a 'plateau' in the velocity distribution at $q \simeq 0.4 - 0.7$ the bulk of matter expanding somewhat slower than in model N32 which has the same $< v >$. The large amount of matter with moderate velocities (compare Figs. 14 and 15 with Fig. 12) causes larger diffusion times for the central region, increases the column density and decreases the effective expansion rate of the ejecta inside the photosphere. However, the rise time to maximum in model PDD3 does not exceed that of model N32 by very much. The reason is that in model PDD3 ^{56}Ni is present closer to the surface than in model N32, which tends to lower the rise time. The net result is that in model PDD3 the rise time is only $t_{bol} \simeq 15$ days. The correlations discussed above also hold for model PDD3 (see Figs. 23-28) and overall it is quite similar to model N32. From an observational point of view model PDD3 can mainly be distinguished on the basis of spectra by measuring the photospheric velocity as a function of time (Fig. 18).

The progenitor of model PDD3 has a mass of 1.4 $M_\odot$. The mass of the envelope formed during the pulsation is $\simeq 0.15\, M_\odot$. A further increase of the rise time is possible, if the envelope mass is increased. However, in the framework of the delayed detonation scenario this is hardly possible. The total mass of the progenitor is limited by the Chandrasekhar mass and an increase of the envelope mass will automatically decrease the mass of the exploding core. Consequently, the amount of ^{56}Ni synthesised during the explosion will be reduced even below the already quite small ^{56}Ni -mass of model PDD3.

A further increase of the rise time to maximum light is achieved with the tamped detonation models DET2ENV. In these models it is assumed that a low density envelope exists prior to the explosion, i.e., the mass of the progenitor is not limited by the Chandrasekhar mass (see Sect. 2.5). Along the sequence of models DET2, DET2ENV2, DET2ENV4 and DET2ENV6 the total kinetic energy and the amount of ^{56}Ni synthesized during the explosion are the same. The average expansion velocity for these models decreases, however, from 1.03 10^9 cm/s for model DET2 to 8.2 10^8 cm/s for model DET2ENV6 due to the increase of the total mass of the configuration (degenerate core + envelope) from 1.2 to 1.8 $M_\odot$, respectively. The mass of matter outside the ^{56}Ni -core also gradually increases from model DET2 to model DET2ENV6. Thus along the DET2ENV sequence the expansion rate and the ^{56}Ni -distribution act in the same direction giving rise to a strict correlation between t_{bol} and $< v >$ (Fig. 25a). This correlation does not coincide, however, with the corresponding correlation for the models DET1, N21, N32, PDD3, DET2 and DF1, although model DET2ENV2 can be assigned to both sequences. The different correlations can be understood as follows: The range of variation of $< v >$ for the models DET2ENV is larger, because of the substantial variation of the mass of the progenitor. Due to the interaction with the envelope the expanding matter is decelerated and the velocity distribution shows a plateau, i.e., in these models the bulk of matter moves with rather low velocity and most of the kinetic energy is concentrated in the very high velocity outer layers (Figs. 8-10). In addition, in the low density detonation models radioactive ^{56}Ni is located closer to the center than in other models having a similar value of $< v >$, i.e., their rise time to maximum light is larger. The rise time increases with mass and reaches a value of $\simeq 20$ days for model DET2ENV6.

For the low density detonation models L_{bol} is increasing with $< v >$ (Fig. 26a) the slope differing from that of the "standard" models, because the diffusion time scales are increasing with mass, i.e., due to the envelope the diffusion time scales become larger and the maxima are "smeared out" in time. However, the relation between t_{bol} and L_{bol} is the same as that of the "standard" models (Fig. 27a).

3.4. Monochromatic light curves

In general, light curve measurements are only available in a few wavelength bands, in particular in the U, B and V band of Johnson's system (1966). Therefore, it is important to calculate monochromatic light curves, too. Because monochromatic LC reflect the energy distribution of the radiation field, they can be expected to be much more sensitive to the physical assumptions made in the LC models. A detailed discussion of this topic including the use of expansion opacities for the line forming region can be found in H2 and Höflich et al. (in preparation). To obtain the results presented below we have calculated the colors for a given density, temperature and velocity structure restricting our radiation transport scheme to the U, B and V band (see H2). Each frequency band is resolved with 100

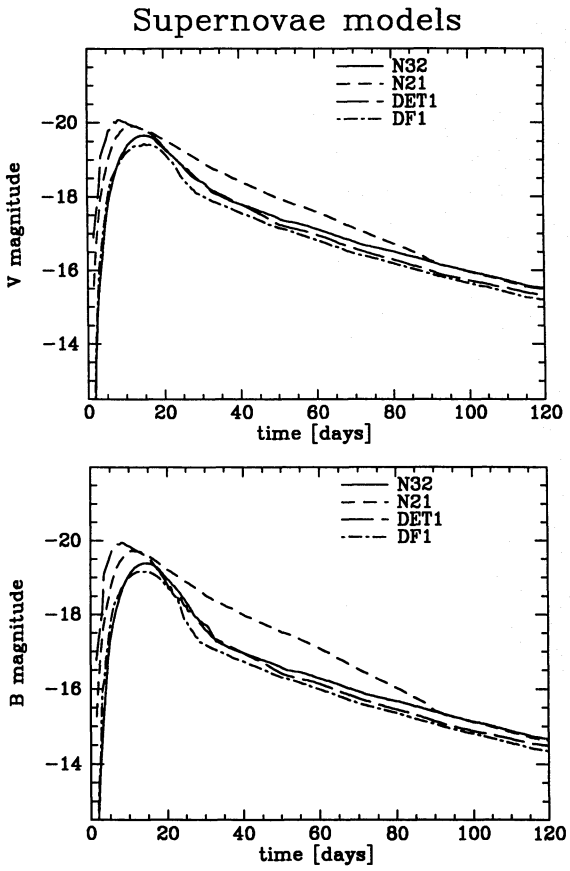

Fig. 30. Monochromatic light curves in the V (a; top) and B (b; bottom) band as a function of time for models N21, N32, DF1 and DET1

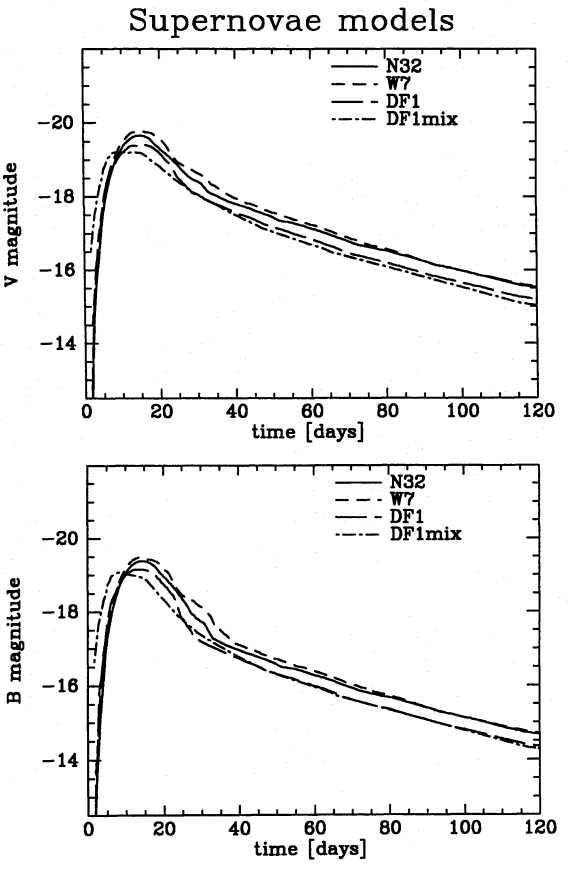

Fig. 31. Same as Fig. 30 but for models N32, W7, DF1 and DF1mix

frequency points, and each band is divided into 16 frequency sub-bands over which the expansion opacity is averaged. For model N21 a more detailed investigation of uncertainties arising from these assumptions can be found in Höflich et al. (in preparation), where a multi-group radiation transport scheme is used and where the effects of the use of an expansion opacity are discussed in comparison with detailed non-LTE atmosphere calculations (at several selected epochs). Here, we only want to report the basic result: *As long as individual lines do not govern the flux in the relevant frequency band the approach used in the present work gives good results*. Consequently, the error in V always remains small ($\Delta m \leq 0.1 mag$), whereas the error in B becomes large ($\Delta m \approx 0.5^m$) at times later than day 50. Therefore, the following results are reliable in the V band and during early epochs in the B band.

The monochromatic LC in the B and V band for the first 120 days are shown in Figs. 30-32 and some related characteristic quantities are given in Table 5. Our models reach a maximum in B and V of $-19.57^m \pm 0.5^m$ and $-19.57^m \pm 0.4^m$, respectively. The time of maximum light ranges from 8.5 days for model DET1 to 21.8 days for model DET2ENV6 (see Table 5). The delay between bolometric and visual maximum typically is about 1 to 3 days. Note, that this delay is consistent with observations (see, e.g., Leibundgut et al. 1991b). In general, the maxima in B and V are broader and more pronounced than in L_{bol} due to temperature effects, in particular, if the maximum of the energy distribution coincides with the corresponding wavelength band (see model N32 in Fig. 30).

The slope of the monochromatic light curves and the basic correlations between observable light curve quantities can be understood in an analogous way as for the bolometric light curves, e.g., t_{bol} and t_V, or L_{bol} and M_V as a function of $< v >$ and M_{Ni} (compare Figs. 25/33 and Figs. 26/34). A new aspect which enters the discussion is the change of temperature in the optically thin region, i.e., in the photosphere, which similarly affects both the color temperature B-V and the absolute fluxes. As a result some additional or stronger correlations between observable quantities exist for monochromatic light curves. In particular, the systematic decrease of temperature with time results, independent of the specific model, into a systematic shift of the frequency distribution of the flux from the UV to the red. This mechanism has very important implications for the maximum brightness in the V band.

M_V as a function of M_{Ni} and $< v >$ in shown in Fig. 34. Obviously, the average expansion velocity has some influence on the maximum brightness in V and on the color index B-V at time t_V. Surprisingly, all models with a significant amount of IME in the observed velocity range (models N21, N32, DET2 and W7) show a very weak dependence ($M_V = -19.68^m \pm 0.12^m$) on the ^{56}Ni -mass (Fig. 34b). This can be understood from the

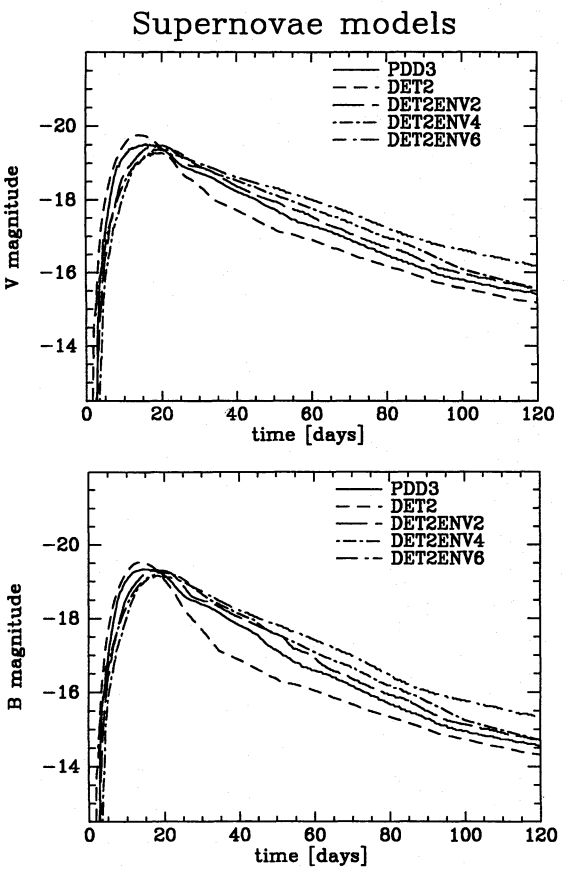

Fig. 32. Same as Fig. 30 but for models PDD3, DET2, DET2ENV2, DET2ENV4 and DET2ENV6

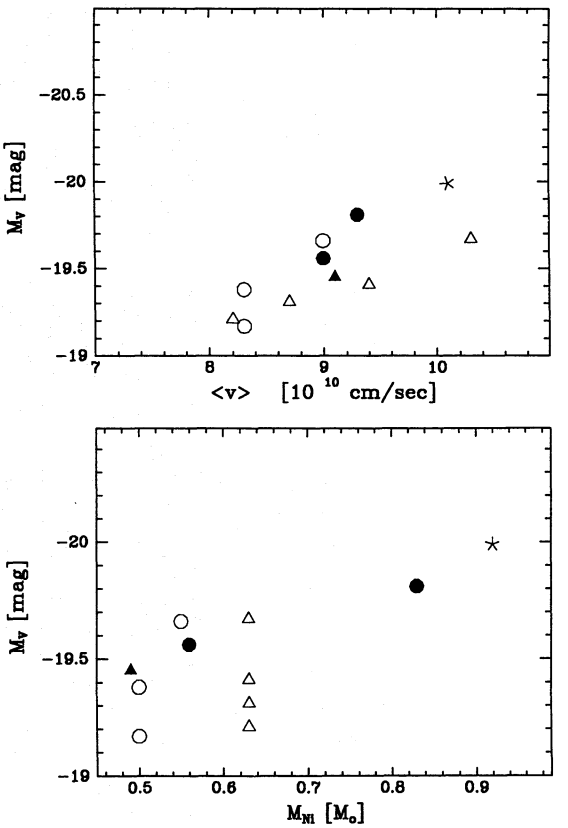

Fig. 34. Same as Fig. 33 but for the absolute visual magnitude M_V

systematic change of temperature with time. For models with a rapidly rising LC (e.g., model N21) the temperature at the photosphere is high, i.e., most of the energy is radiated in the UV and just a small fraction is emitted in the V band. On the other side with increasing t_V (models DET2, W7 and N32) the maximum of the flux distribution is shifted towards the V band, i.e., there exist two counteracting effects of similar size. The uncertainties within this class of models (which all produce a significant amount of IME) can be eliminated even further using the correlation between M_V and $< v >$ (Fig. 34a) and v_{phot} and M_V (Fig. 35), respectively. The tendency of equilibrating M_V ($\Delta M_V \approx 0.23$ while $\Delta m_{bol} \approx 0.36$) can also been seen for the detonation model DET1. The significantly smaller brightness in V for the deflagration models DF1 and DF1MIX are mainly due to a low L_{bol} (see above). However, these latter three models can easily be discriminated using their spectra (i.e., chemical

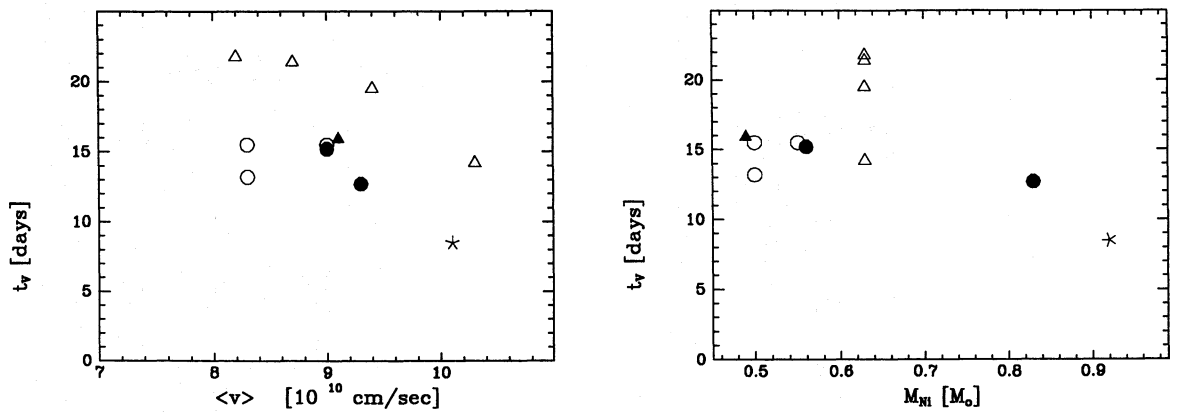

Fig. 33. Rise time to visual maximum t_V as a function of (a; top) the average expansion velocity $< v >$, and (b; bottom) of the ^{56}Ni -mass M_{Ni} for all investigated explosion models. Symbols have the same meaning as in Fig. 25

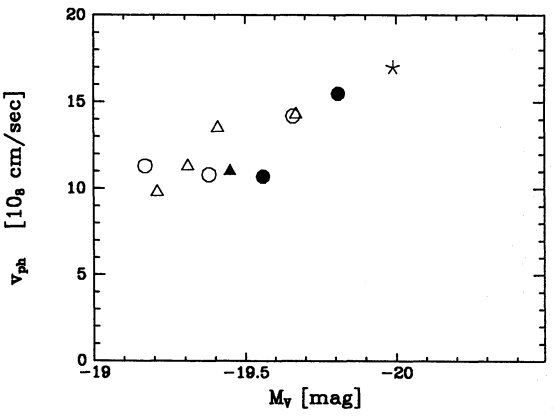

Fig. 35. Photospheric velocity at the time of visual maximum $v_{phot}(t_V)$ as a function of the absolute visual magnitude M_V. Symbols have the same meaning as in Fig. 25

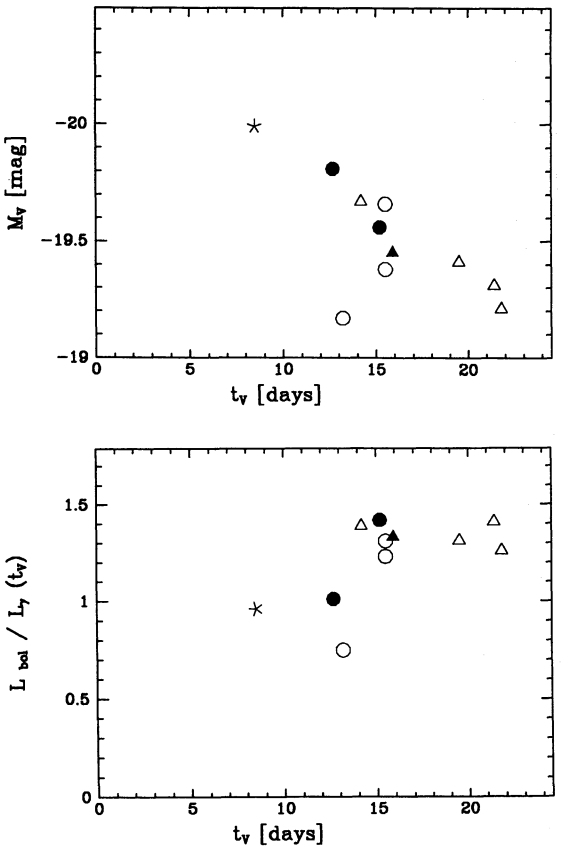

Fig. 36. Rise time to visual maximum t_V as a function of the absolute visual magnitude M_V (a; top), and the ratio of the visual and gamma-ray luminosity at visual maximum $L_V/L_\gamma(t_V)$ as a function of t_V (b; bottom). Symbols have the same meaning as in Fig. 25

composition) and the relation between M_V and $< v >$ or v_{phot} (Figs. 34a and 35). Finally note that we find a similar small spread in M_V ($M_V = -19.32^m \pm 0.15$) for the class of tamped detonation models. Here, besides the discussed temperature effect also the larger relative energy input due to the increasing mass of the shell compensates the (absolutely) lower decay rate at later epochs and equilibrates M_V.

Finally note, that t_V is well correlated to the absolute visual magnitude (Fig. 36a) for the same reasons as already discussed for the bolometric LC (see Fig. 27a) and that $L_V/L_\gamma(t_V)$ (Fig. 36b) shows a similar behaviour as its bolometric analogue (see Fig. 29).

4. Final discussion and conclusion

Different explosion mechanisms for SNe Ia have been studied by means of hydrodynamical models which take a detailed description of nuclear processes into account. Our investigation covers models of detonations, deflagrations and delayed detonations. Besides these standard explosion models, the effect of mixing, stellar pulsations and the interaction of the exploding white dwarf with an extended envelope have been investigated. The interaction between the extended envelope leads to the formation of a thin dense shell.

A sophisticated LC model was used to study the influence of the different explosion models on the thermal cdbec% ture of the expanding ejecta. We find that varying the time-dependent opacity by a factor of two only weakly influences the LC ($\Delta t_{bol} \approx \pm 1 day$) due to the strong temperature dependence of the opacity at temperatures below $\approx 2\ 10^4$ K. This result is in strict contrast to the finding of Shigeyama et al. (1992; see also H2) that an arbitrary adjustment of a *constant* opacity can change the early slope and rise time of SN Ia LCs by up to 80% if the opacity is changed by a factor of ± 2. Thus, uncertainties in the opacity due to poorly known oscillator strengths of line transitions and due to the incompleteness of our line list are not influencing our results.

The differences between the bolometric light curves of our models can be understood in terms of the expansion rate of the ejecta, the total energy release, the distribution of the radioactive matter, and the total mass and density structure of the envelope: The expansion rate of the ejecta governs the change of the background model with time, the energy release by the radioactive decay of ^{56}Ni and ^{56}Co provides the dominant energy source, the distribution of the radioactive material determines both the location and the amount (via the γ-ray escape probability) of the energy input, and finally the total mass and the density distribution of the expanding ejecta influence the diffusion time scale.

We find that rise times to bolometric (t_{bol}) and visual (t_V) maximum significantly longer than 15 and 17 days, respectively, are hardly to obtain provided the progenitor star is a C/O white dwarf of about 1.2 to 1.4 $M_\odot$. The limitation of the maximum rise time is due to a causal connection between the amount of matter which has undergone nuclear fusion and the expansion rate, because the energy released during nuclear burning is transfered into expansion energy within less than an hour. According to observations the minimum amount of ^{56}Ni a reasonable model should produce is $\approx 0.4 \ldots 0.5 M_\odot$ (Branch & Tammann 1992;

Leibundgut et al. 1991b), which sets a lower limit for the expansion rate. One way out of this dilemma would be to produce less kinetic energy by starting from a progenitor with less energetic fuel, e.g., a more oxygen-rich C/O white dwarf or an O-Ne-Mg white dwarf (which however is more likely to collapse than to explode; see Isern et al. 1991). But even then the explosion energy would be lower at most by $\approx 10\%$ (25% for an O-Ne-Mg dwarf) implying a change of the mean velocity of $\lesssim 5\%$ (12% for an O-Ne-Mg dwarf), only. Taking our relation between $< v >$ and t_{bol} into account, this would change t_{bol} only by one or two days. Therefore, a more oxygen-rich C/O white dwarf cannot be regarded as a solution, whereas an O-Ne-Mg white dwarf could solve the problem provided it does not collapse.

In fact we must turn to models where an interaction of the expanding ejecta with a low density envelope occurs, which can increase the rise time t_{bol} from 15 up to 20 days. Such an envelope may be created by a large scale pulsation of the white dwarf during the burning stage (model PDD3) or can be imagined to exist according to the merger scenario prior to the explosion ("tamped detonation" models DET2ENV). The envelope absorbs a significant amount of the kinetic energy and decelerates the expanding matter inside the envelope. This results in a re-distribution of the kinetic energy within the ejecta which eventually consists of an outer high velocity region and an inner region or a thin shell which is slowly expanding. The lower expansion rate of the inner region enlarges the diffusion time scales and, consequently, produces a slower light curve.

Several correlations between observable quantities such as L_{bol}, t_{bol}, M_V and t_V on one side and model specific quantities such as the mean expansion velocity $< v >$ and the ^{56}Ni -mass on the other side have been found. Some of these correlations allow for a discrimination of models, e.g., the correlation between the maximum bolometric luminosity L_{bol} and the ^{56}Ni -mass (see Fig. 26b). Other correlations show that certain observable quantities are almost model independent, e.g., the maximum brightness in the V filter (see Fig. 34b). Finally, there exist correlations between two observable quantities, e.g., between time of visual maximum t_V and the absolute visual magnitude M_V, which can be used for a distance determination. However, several correlations either are not strictly valid or can only be applied within a subset of explosion models. In the latter case independent observations (i.e., spectra) or correlations are required to determine the proper subset. For example, the pulsating delayed detonation and tamped detonation models do not follow several of the correlations which are valid for the standard explosion scenarios. However, these two subsets of models can easily be separated by the change of the photospheric velocity v_{phot} as a function of time. In the pulsating delayed detonation and tamped detonation models the photospheric velocity shows a distinct plateau phase starting at maximum light during which v_{phot} is almost constant for up to several weeks. In fact, the width of the plateau provides an estimate of the mass of the extended envelope. In the standard models the plateau does not exist, i.e., v_{phot} is continuously decreasing with time.

Based on his analytical models with a constant opacity, Arnett (1979; see also Arnett et al. 1985) noticed that the luminosity at maximum light is very close to the rate of energy deposition by gamma-rays at that time. We find that, depending on the explosion model, this 'rule' is violated by up to 50% if a realistic opacity is used. The difference between the analytical and our numerical models arises from the temperature dependence of the opacity. A change of opacity with temperature implies a time sequence, because in all models the ejecta monotonically become cooler with time. If now at about maximum light the opacity drops (for temperatures below $\simeq 2\ 10^4$ K) or increases (for $T \gtrsim 2\ 10^4$ K), the photosphere retreats faster or slower (in mass), respectively, than in the case of a constant opacity. Consequently, more ($A_{bol} > 1$) or less ($A_{bol} < 1$) than the energy deposited at a given epoch can be radiated (see Sect. 3.3.2).

In the literature SNe Ia are often used as standard candles for the determination of extragalactic distances, because SNe Ia are sufficiently bright events. Therefore, they can provide a measurement of the Hubble constant (see, e.g., Branch 1982). In this respect the small variation in M_V found by us ($M_V \approx -19.2^m \ldots -20.0^m$) may be of some interest. In fact, within subsets of models the uncertainty in M_V is much smaller, i.e., M_V hardly depends on the specific model ($\Delta M_V \approx 0.1^m$). All models which produce some amount of intermediate mass elements and in which the photospheric velocity is continuously decreasing with time (i.e., the standard models) show a maximum brightness in V of $M_V = -19.68^m \pm 0.1^m$, while in all non-standard models the visual magnitude at maximum has a value of $M_V = -19.32^m \pm 0.15^m$.

Concerning observations of SNe Ia a tendency may exist that in very slowly rising supernova the photospheric velocity is only slowly varying with time after maximum (e.g., SN1990N; Fillipenko et al. 1992; Leibundgut et al. 1991b), whereas more rapidly rising SNe Ia show a continuously decreasing v_{phot} (SN1981b, SN1972e, 1989b; Barbon et al. 1990; Branch et al. 1988; Graham 1987). However, this point requires further observations and a more detailed comparison between observed and calculated light curves and spectra (Müller et al. , in preparation).

Finally, we want to point out the limits of our LC model. The most restrictive assumption, which is underlying our present LC model, is the use of a grey opacity. This restriction is dropped in our frequency-dependent multi-group light curve calculations, which are in progress. The second most restrictive assumption of LTE, which we use when calculating the frequency-dependent opacity, has been dropped in non-LTE spectral computations (to be published).

Acknowledgements. We would like to thank Kenichi Nomoto for providing us his model W7 in machine readable form.

Appendix A: Flame prescription

A naive straightforward incorporation of the flame prescription of Eq. (1) into a hydrodynamical code leads in some cases to small scale temperature fluctuations and to fluctua-

tions of the chemical abundances of up to $\sim 30\%$ in low density ($\rho \simeq 10^7 \mathrm{gcm}^{-3}$) regions. The fluctuations are not caused by numerical instabilities or numerical errors, but are due to intrinsic difficulties of the simulation of a deflagration wave using coarse computational grids.

For deflagrations the spatial scale (the thickness of the wave, l_{def}) is related to the corresponding time scale (burning time, τ_n) as $l_{def} \simeq (k \cdot \tau_n)^{1/2}$, where k is the temperature conductivity. For a degenerate C/O mixture with $\rho \simeq 10^9 \mathrm{gcm}^{-3}$one has $\tau_n \sim 10^{-10}$ s and $l_{def} \sim 10^{-3}$ cm. For a computational cell the burning time scale is equal to τ_n (by order of magnitude). The spatial scale, however, is the size of a cell, $\delta R \simeq 10^{5-6}$ cm assuming a typical total number of cells $N \sim 10^{2-3}$. Thus, the ratio $\delta R / l_{def}$ is $\sim 10^{8-9}$. As long as this ratio remains larger than ~ 1 the continuous propagation of the deflagration wave is replaced in computations based on finite-differences by a sequence of nearly constant volume explosions of computational cells. These explosions occur with a frequency $\sim D_{def}/\delta R$ and generate pressure waves with amplitudes which are close to those produced by the shock resulting from the decay of a discontinuity separating unburnt and isochorically burnt matter. An increase of N leads to a corresponding increase of the frequency, but does not influence the amplitude of the pressure waves.

The propagation of the pressure waves back and forth inside the expanding white dwarf creates a complicated pattern of fluctuations of density, pressure and velocity in the unburnt matter. During the subsequent propagation of the detonation wave (in delayed detonation models) these fluctuations result in strong fluctuations of the temperature behind the wave and, consequently, in fluctuations of the abundances. Since it is impossible to increase the numerical resolution by $\sim 8-10$ orders of magnitude, the only possibility to eliminate the fluctuations in the computations is to artificially increase the time scale of burning. Thus, in this study (as well as in Khokhlov 1991b) the following computational strategy is adopted. We use (only for the deflagration stage of the flame propagation) an artificial limiting for the $^{12}C + ^{12}C$ reaction rate, F_c, and for the NSQE relaxation time scale, τ_{NSQE},

$$F_{c,lim} = F_c \,/\, (1 + \tau_{lim} F_c Y_c) \quad , \qquad (A1)$$

$$\tau_{NSQE,lim} = \tau_{NSQE} + \tau_{lim} \quad , \qquad (A2)$$

where

$$\tau_{lim} = C_{lim}\,(\delta R / a_s) \quad , \qquad (A3)$$

with $C_{lim} = 10$. Y_c is the ^{12}C mole fraction (for a definition of τ_{NSE} and F_c see Khokhlov 1991a). The use of Eqs. (A1-A3) somewhat reduces the fluctuations and leads to relatively smooth final abundance distributions, but does not noticeably affect the final density and velocity distributions.

References

Arnett, W.D., 1969, Ap&SS 5, 180
Arnett, W.D., 1979, ApJ 230, L37
Arnett, W.D., Branch, D., Wheeler, J.C., 1985, Nature 314, 337
Barbon, R., Benetti, S., Cappellaro, E., Rosino, L., Turatto, M. 1990, A&A 237, 79
Benz, W., Bowers, R.L., Cameron, A.G.W., Press, W.H., 1989, ApJ 348, 647
Branch, D., 1982, ApJ 248, 1076
Branch, D., 1992, ApJ 392, 35
Branch, D., Tammann, G.A., 1992, Type Ia Supernovae as Standard Candles, Prep. No. 46, University of Basel
Branch, D., Drucker, W., Jeffery, D., 1988, ApJ 330, L117
Isern, J., Canal, R., Labay, J., 1991, ApJ 372, L83
Chechetkin, V.M., Gershtein, S.S, Imshennik, V.S., Ivanova, L.N., Khlopov, M.Yu., 1980, Ap&SS 67, 61
Colgate, S.A., McKee, C., 1969, ApJ 157, 623
Fillipenko, A.V., Richmond, M.W., Matheson, T., Shields, J.C., Burbidge, E.M., Cohen, R.D., Dickinson, M., Malkan, M.A., Nelson, B., Pietz, J., Schlegel, D., Schmeer, P., Spinrad, H., Steidel, C.C., Tran, H.D., Wren, W., 1992, ApJ 384, L15
Fuller, G.M., Fowler, W.A., Newman, M.J., 1982 ApJS 270, 123
Graham, J.R., 1987, ApJ 318, L47
Hachisu, I., Eriguchi, Y., Nomoto, K., 1986, ApJ 308, 161
Hansen, C.J., Wheeler, J.C., 1969 Ap&SS 3, 464
Höflich, P., Khokhlov, A., Müller, E., 1991, A&A 248, L7
Höflich, P., Khokhlov, A., Müller, E., 1992a, A&A 259, 549
Höflich, P., Müller, E.; Khokhlov, A., 1992b, A&A, in press
Iben, I.Jr., Tutukov, A.V., 1984, ApJS 54, 335
Imshennik, V.S., Khokhlov, A.M., 1984, Sov. Astron. Lett. 10, 262
Ivanova, L.N., Imshennik, V.S., Chechetkin, V.M., 1974, Ap&SS 31, 497
Ivanova, L.N., Imshennik, V.S., Chechetkin, V.M., 1977, Astron. Zhurn. 54, 354
Ivanova, L.N., Imshennik, V.S., Chechetkin, V.M., 1982, SvAL 8, 8
Ivanova, L.N., Imshennik, V.S., Chechetkin, V.M., 1983, ITEP-preprint, No.109
Johnson, H.L., 1966, ARA&A 4, 197
Karp, A.H., Lasher, G., Chan, K.L., Salpeter E.E., 1977, ApJ 214, 161
Kirshner, R., Kwan, R., 1974 ApJ 193, 27
Khokhlov, A., 1989, Sov. Sci. Rev. E. 8, 1
Khokhlov, A., 1991c, A&A 245, L25
Khokhlov, A., 1991b, A&A 245, 114
Khokhlov, A., 1991a, A&A 246, 383
Khokhlov, A., Müller, E., Höflich, P., 1991, A&A 253, L9
Kurucz R.L., 1988, in: Proceedings of the IAU conference, Baltimore, and private communication
Leibundgut, B., Tammann, G.A., 1990, A&A 230, 81
Leibundgut, B., Kirshner, B., Filippenko, A.V., Shields, C., 1991a, ApJ 371, L23
Leibundgut, B., Tammann, G.A., Cadonau, R., Cerrito, D., 1991b, CFA preprint No. 3172
Mochkovitch, R., Livio, M., 1989, A&A 209, 111
Mochkovitch, R., Livio, M., 1990, A&A 236, 378
Müller, E., Arnett, W.D., 1982, ApJ 261, L109
Müller, E., Arnett, W.D., 1986, ApJ 307, 619
Müller, E., Höflich, P., 1991, in: SN1987A and Other Supernovae, eds. I.J. Danziger and K. Kjär, ESO, Garching, p.379
Müller, E., Höflich, P., Khokhlov, A., 1991a, A&A 249, L1
Müller, E., Fryxell, B.A., Arnett, D., 1991b, A&A 251, 505

Nomoto, K., 1982, ApJ 253, 798
Nomoto, K., Sugimoto, D., 1977, PASJ 29, 765
Nomoto, K., Sugimoto, D., Neo, S., 1976, Ap&SS 39, 137
Nomoto, K., Thielemann, F.-K., Yokoi, K., 1984, ApJ 286, 644
Paczyński, B., 1985, in: Cataclysmic Variables and Low-Mass X-Ray Binaries, eds. D.Q. Lamb, J. Patterson, Reidel, Dordrecht, p.1
Shigeyama, T., Nomoto, K., Hitoshi, Y., Thielemann, F.-K., 1992, ApJ Lett., in press
Sutherland, P.G., Wheeler, J.C., 1984, ApJ 280, 282
Takahashi, K., ElEid, M.F., Hillebrandt, W., 1978 A&A 67, 185
Webbink, R.F., 1984, ApJ 277, 355
Wheeler, J.C., Harkness, R.P., 1990, Rep. Prog. Phys. 53, 1467
Woosley, S.E., 1990, in: Supernovae, ed. A.G.Petscheck, Springer-Verlag, New York, p.182
Woosley, S.E., Timmes, 1992, ApJ, in press
Woosley, S.E., Weaver, T.A., 1986, ARAA 24,
Woosley, S.E., Weaver, T.A., 1992, in: Supernovae, eds. J. Audouze, S. Bludman, R. Mochkovitch and J. Zinn-Justin, Elsevier, in press
Woosley, S.E., Taam, R.E., Weaver, T.A., 1986, ApJ. 301, 601
Yamaoka, H., Nomoto, K., Shigeyama, T., Thielemann, F.K., 1992, Univ. Tokyo preprint No.92-1, and ApJ submitted

Note added in proof: Concerning the numerical stability of the implicit hydrodynamical code of Nomoto et al. (1984; see Sect. 2.3) we point out that according to Nomoto (private communication) "their hydro-code is capable to calculate with any time step, both much longer and much shorter than the CFL time step, i.e. the code is stable for any time step if a staggered mesh is used." This fact was proved in Sugimoto et al. (1981; Prog. Theor. Phys. Suppl., No. 70, p. 115).